

1 **Revision 2 Potential Link between Antigorite Dehydration and**
2 **Shallow Intermediate-Depth Earthquakes in Hot Subduction Zones**

3 TONGBIN SHAO^{1,2,3*}, MAOSHUANG SONG^{1,3*}, XI MA², XING DING^{1,3},
4 SHIRONG LIU⁴, YONGSHENG ZHOU², JIE WU⁵, XIAONING WANG^{1,3},
5 JIANFENG LI^{1,3}

6 ¹State Key Laboratory of Isotope Geochemistry, Guangzhou Institute of Geochemistry,
7 Chinese Academy of Sciences, Guangzhou 510640, China

8 ²State Key Laboratory of Earthquake Dynamics, Institute of Geology, China
9 Earthquake Administration, Beijing 100029, China

10 ³CAS Center for Excellence in Deep Earth Science, Guangzhou 510640, China

11 ⁴State Key Laboratory of Environmental Geochemistry, Institute of Geochemistry,
12 Chinese Academy of Sciences, Guiyang 550003, China

13 ⁵College of Earth Sciences and Guangxi Key Laboratory of Hidden Metallic Ore
14 Deposits Exploration, Guilin University of Technology, Guilin 541004, China

15 *Corresponding author: tshao@gig.ac.cn (T. Shao), msong@gig.ac.cn (M. Song)

16 **ABSTRACT**

17 The distribution of earthquakes at intermediate depths corresponding to pressures
18 <2 GPa in several hot subduction zones (such as Cascadia and southwestern Japan)
19 coincides with the breakdown of antigorite to forsterite and talc; thus, this reaction may
20 have triggered these earthquakes. However, previous studies have overlooked the

21 potential significance of this reaction. Here, we performed a series of time-dependent
22 dehydration experiments on antigorite at a pressure of 200 MPa and temperature range
23 of 500-650 °C. The results show that dehydration is controlled by a heterogeneous
24 nucleation and growth mechanism and has an activation energy of 354 ± 24 kJ/mol. The
25 formation of fine-grained forsterite and large talc crystals is consistent with kinetic
26 results indicating Avrami exponents $n \sim 1.4-1.1$ and ~ 2.7 , respectively. Fluid
27 production rates at 600 and 650 °C are 2.54×10^{-6} and $4.69 \times 10^{-5} \text{ m}_{\text{fluid}}^3 \text{ m}_{\text{rock}}^{-3} \text{ s}^{-1}$,
28 respectively, which are much faster than those of mantle deformation, causing high
29 fluid pressure in hot subducting mantle but not necessarily embrittlement. We
30 emphasize the role of kinetic mechanisms in controlling the sizes of reaction products,
31 which likely determine the mechanical behavior of serpentized fault zones.
32 Superplasticity or velocity weakening of fine-grained forsterite and velocity weakening
33 of antigorite by water and/or talc may be responsible for earthquake nucleation and
34 propagation in a heterogeneous system, which can be either dehydration products
35 within a serpentized fault zone or the mixture of antigorite fault and surrounding
36 peridotite in hot subduction zones (<2 GPa).

37

38 **Keywords:** Antigorite; Talc; Forsterite; Kinetic mechanism; Subduction zone;
39 Shallow intermediate-depth earthquakes

40

41

INTRODUCTION

42 Serpentine is a main hydrous phase in oceanic plates and the most abundant

43 water-bearing mineral in altered ultramafic rocks (Hyndman and Peacock, 2003), with
44 water contents up to ~13 wt.% (Schmidt and Poli, 1998; Shao et al., 2014, 2021; Ulmer
45 and Trommsdorff, 1999). There are three main forms of serpentine: chrysotile, lizardite,
46 and antigorite (Rinaudo and Gastaldi, 2003). Among them, antigorite is persistent in
47 subduction zones to a depth of ~200 km and is thus called high-temperature serpentine
48 (Ji et al., 2013; Reynard, 2013; Reynard et al., 2007; Shao et al., 2014). Previous
49 studies have shown that the temperature stability field of antigorite, from 1 to 5 GPa, is
50 close to the isotherm of the lower plane of a double seismic zone (DSZ) (e.g., Abers et
51 al., 2013; Peacock, 2001; Yamasaki and Seno, 2003), which means that the hypocenter
52 distribution of intermediate-depth earthquakes in the subducted mantle fits the
53 distribution of antigorite. However, a recent study by Ferrand (2019) suggested that
54 many of the upper-plane earthquakes actually appear in the uppermost mantle, as
55 clearly evidenced for northern Chile. Therefore, antigorite dehydration is commonly
56 used to explain the seismic activity in the entire DSZ (Dobson et al., 2002; Omori et al.,
57 2004; Peacock, 2001).

58 In a pioneering study by Raleigh and Paterson (1965), seismogenic faulting is
59 claimed to be triggered within the dehydrating antigorite itself due to fluid
60 overpressure. This is the original model of so-called ‘dehydration embrittlement’,
61 which is possible only when the Clapeyron slope of serpentine dehydration is positive
62 (i.e., at $P < \sim 2$ GPa). However, several experimental studies on syndeformational
63 antigorite dehydration have found that antigorite is weakened but deforms aseismically
64 (Chernak and Hirth, 2010, 2011; Gasc et al., 2011, 2017; Okazaki and Hirth, 2016;

65 Proctor and Hirth, 2015; Shao et al., 2021), which might be comparable to slow
66 earthquakes occurring in hot subduction zones (e.g., Chernak and Hirth, 2010; French
67 et al., 2019; Okazaki and Katayama, 2015). Some studies have improved the model
68 and considered that seismogenic faulting should occur in more brittle surrounding
69 rocks rather than the dehydrating antigorite itself (e.g., Brantut et al., 2017; Ferrand et
70 al., 2017). For example, Ferrand et al. (2017) proposed dehydration-driven stress
71 transfer (DDST) to generate earthquake events in fresh peridotite at the edge of
72 antigorite-rich zones. However, seismicity is triggered by dehydration of very limited
73 amounts of antigorite (Ferrand et al., 2017; Xia, 2013), implying that these earthquakes
74 are not the result of fluid overpressure. Concurrently, Brantut et al. (2017) proposed a
75 new dehydration embrittlement model, in which a positive feedback between pore fluid
76 pressure, shear compaction, and the dehydration rate of antigorite was considered to
77 induce nucleation and propagation of earthquakes in the surrounding rocks forming the
78 subducted slab. Thus, the role of fluid in triggering the lower plane earthquakes is still
79 inconclusive. Furthermore, both the DDST and the new dehydration embrittlement
80 models, unlike the original dehydration embrittlement, are specifically for the case
81 where the net volume change of the dehydration reaction is negative. These facts
82 suggest that none of the models can explain seismicity related to the dehydration
83 reaction of antigorite with positive volume change, which is the reaction of antigorite
84 breakdown to forsterite and talc.

85 To explain intermediate-depth earthquakes, several dehydration kinetics studies of
86 serpentine minerals have been performed over the past two decades using various

87 methods, such as time-resolved X-ray diffraction (XRD) (Chollet et al., 2011; Gualtieri
88 et al., 2012; Inoue et al., 2009; Perrillat et al., 2005), high-temperature infrared
89 microspectroscopy (Sawai et al., 2013), and thermogravimetric analysis (Balucan et al.,
90 2011; Liu et al., 2019; Weber and Greer, 1965). However, published conclusions
91 regarding the kinetic mechanism are significantly different (Balucan et al., 2011;
92 Gualtieri et al., 2012; Liu et al., 2019; Perrillat et al., 2005; Sawai et al., 2013). In
93 addition, these studies were conducted under conditions of either ambient pressure
94 (e.g., Liu et al., 2019; Sawai et al., 2013) or high pressures [e.g., 1.1-1.5 GPa in
95 Perrillat et al. (2005) and ~4 GPa in Chollet et al. (2011)], but data under relatively low
96 pressures (<1 GPa) are lacking. Furthermore, no microstructural observations of run
97 products were performed in most of these previous studies to support their analyses of
98 the kinetic mechanism of antigorite dehydration. These previous dehydration kinetics
99 studies all suggest that antigorite dehydration can trigger earthquakes based on either
100 the original dehydration embrittlement (related to fluid overpressure) (e.g., Chollet et
101 al., 2011; Perrillat et al., 2019) or the DDST model (Liu et al., 2019). According to the
102 results of syndeformational dehydration experiments with antigorite (e.g., Chernak and
103 Hirth, 2011; Gasc et al., 2011), however, fast fluid production rates calculated based on
104 kinetic parameters alone cannot account for the potential link between antigorite
105 dehydration and seismicity (e.g., Liu et al., 2019; Perrillat et al., 2005). The
106 microstructural morphology (controlled by the kinetic mechanism) and thus the
107 mechanical behavior of reaction products should not be ignored. In addition, the
108 reaction of antigorite breakdown to forsterite and talc has not yet been considered in

109 most of these dehydration kinetics studies (e.g., Chollet et al., 2011; Inoue et al., 2009;
110 Liu et al., 2019; Perrillat et al., 2005). This reaction fits most shallow
111 intermediate-depth seismicity in hot subducting mantle beneath Cascadia and
112 southwestern Japan (Abers et al., 2013; Ferrand, 2019), indicating the geophysical
113 significance of this dehydration reaction.

114 In this paper, high-pressure and high-temperature (high-*PT*) experiments were
115 carried out on antigorite using a Tuttle-type autoclave (cold-seal hydrothermal vessel).
116 Our goal is to study the dehydration kinetics of antigorite by isothermal experiments
117 and analyze the kinetic mechanism by both Avrami modeling of the experimental data
118 and microstructural observations of run products, which provide constraints on the
119 fluid production rate and the mechanical behavior of run products, respectively. Finally,
120 the experimental results are extrapolated to hot subduction zones ($P < 2$ GPa) to
121 interpret the shallow intermediate-depth seismicity occurring in these zones by
122 emphasizing the role of the kinetic mechanism in controlling the size and, thus,
123 mechanical behavior of dehydration products.

124

125

METHODS

126 **Starting Material**

127 The material used in the dehydration kinetics experiments is known as Xiuyan
128 jade in Chinese culture, has a mineral composition of mainly antigorite with trace
129 amounts of dolomite and apatite (<1%), and was collected from Xiuyan Manchu

130 Autonomous County (Liaoning Province, China) (Shao et al., 2014, 2021). Whole-rock
131 X-ray fluorescence (XRF) analyses reveal that the starting material contains 44.25
132 wt.% SiO₂, 41.83 wt.% MgO, 0.28 wt.% CaO, 0.03 wt.% Na₂O, 0.06 wt.% Al₂O₃, 0.97
133 wt.% TFeO (total iron given as FeO), and 12.19 wt.% water. The nearly pure antigorite
134 crystals were crushed and ground into powder with various grain sizes, from which
135 mean particles of ~10-15 μm were selected and stored in a furnace at 110 °C,
136 eliminating absorbed molecular water. To determine the structure of the starting
137 material that may affect the phase stability and thus the dehydration kinetics, we
138 investigated the starting material via XRD at the Institute of Geology, China
139 Earthquake Administration (IGCEA), Beijing, and transmission electron microscopy
140 (TEM) at the Institute of Geochemistry, Chinese Academy of Sciences (IGCAS),
141 Guiyang, Guizhou Province. The TEM investigation was carried out on a suspension
142 that was made according to the powder technique described by Shen et al. (2020). The
143 XRD analyses suggest that the starting material is characterized by lattice constants
144 with $a=5.42$ Å, $b=9.24$ Å, $c=7.27$ Å, and $\beta=91.32^\circ$. Figure 1 shows a high-resolution
145 TEM image of a representative grain and a histogram of the m value, which is equal to
146 $(a^*/5.42)\times 2+1$, where a^* is the length of the a-axis and 5.42 Å represents the length of
147 the subcells along the a-axis in this material, that is, the lattice constant a . m represents
148 the number of tetrahedra in a single chain along the wavelength a^* . The results show
149 that the m value ranges from 13 to 18, with the most frequent value being 15; thus, this
150 value can be used as the polysome m value of the starting material.

151 **High-*PT* Experiments**

152 All dehydration kinetics experiments were performed at a pressure of 200 MPa
153 and temperatures of 500-650 °C with durations ranging from 1 to 745.5 hours (h)
154 (Table 1) using a Tuttle-type autoclave (Figure 2) at the Guangzhou Institute of
155 Geochemistry, Chinese Academy of Sciences (GIGCAS). The antigorite powder was
156 loaded into gold capsules of two sizes: one had an outer diameter of 5.0 mm, and the
157 other had an outer diameter of 4.6 mm. Both gold capsules had a wall thickness of 0.25
158 mm and a length of 18 mm. Gold is commonly used in high-temperature experiments
159 because it is chemically inert. One side of a capsule was welded with a tungsten inert
160 gas high-frequency pulse welder (PUK3, Lampert Werktechnik, Germany) before
161 loading, and the other side was welded after loading with either just sample powder
162 (the system was water unsaturated at least at the beginning of the experiment) or
163 sample powder plus excess deionized water (the system was water saturated
164 throughout the experiment). A leak check was performed before all experiments. For
165 initially water-unsaturated samples, we immersed capsules in alcohol for at least 1 h
166 and then placed them in a drying furnace at 110 °C for at least 2 h. For water-saturated
167 samples, the capsules were directly placed in the drying furnace at 110 °C for at least 2
168 h. To determine whether the sample capsule was a closed or open system, the sealing
169 conditions of the sample capsule had to be confirmed. Thus, it was necessary to weigh
170 each sample capsule before and after the experiments and compare the weights to
171 determine the sealing conditions. Capsules with a weight difference of $< \sim 0.5$ mg were
172 considered completely sealed, which could be further supported by the increased
173 widths of these capsules after removal from the vessels. Capsules whose shapes stayed

174 the same as before the experiments were considered open, and the experimental results
175 from capsules with this characteristic are not reported in this study. Water-saturated
176 experiments can be further confirmed by the presence of free water in the recovered
177 samples. The capsules were loaded into the bottom of the hydrothermal vessel,
178 followed by a filler rod (~6 cm in length) for the vertical vessel, with the purpose of
179 preventing convection. Pressures were generated by pumping water into the vertical
180 vessel and were measured by a pressure gauge with a precision of ± 10 MPa (Huang et
181 al., 2017). To monitor temperature, an external K-type thermocouple was inserted into
182 a hole near the bottom of the vessel. Temperature was controlled with an accuracy of
183 ± 2 °C. At the end of the experiment, the vessel was chilled by immersion in ice water,
184 thereby decreasing the temperature of gold capsules to < 100 °C within a few seconds.

185 **XRD and Microstructural Observations**

186 After all the high-*PT* experiments, the sample powders were recovered from the
187 capsules and then ground for XRD analysis, except for two complementary
188 experiments from which sample powders (Atg103 at 600 °C and initially
189 water-unsaturated conditions for 48 h and Atg112 at 650 °C and water-saturated
190 conditions for 3 h) were recovered for microstructural observations under a Zeiss
191 Sigma scanning electron microscopy (SEM) system equipped with an Oxford X-Max
192 50^N energy-dispersive X-ray spectroscopy (EDS) detector at Guilin University of
193 Technology (Guangxi Province, China). Powder XRD patterns were obtained with a
194 Bruker D8 ADVANCE X-ray diffractometer at both the GIGCAS and IGCEA. The
195 analyses were operated using Cu K α radiation under a 40 kV target voltage and 40 mA

196 target current. Data were collected over the range of 5-70° 2θ with a step size of 0.02°
197 2θ and a count time of 19.2 s per step. For the analyses, the powder diffraction files
198 (PDF) cards of antigorite (monoclinic) from Hess et al. (1952), forsterite
199 (orthorhombic) from Hushur et al. (2009), and talc (triclinic) from Rayner et al. (1973)
200 were employed. For antigorite, the (001) plane at 2θ=12.114, (002) plane at 2θ=24.503,
201 (201) plane at 2θ=35.597, and (211) plane at 2θ=37.121 were used for comparison with
202 the peaks of the starting material and residual antigorite recovered from the high-*PT*
203 experiments. For forsterite, the (112) plane at 2θ=36.538, (021) plane at 2θ=22.898,
204 (130) plane at 2θ=32.346, (122) plane at 2θ=39.715, (140) plane at 2θ=40.096, and
205 (222) plane at 2θ=52.281 were employed for comparison with the peaks of forsterite
206 formed in the process of antigorite dehydration. For talc, planes (001) and (003) at
207 2θ=9.447 and 28.605, respectively, were basically consistent with the peaks of talc in
208 the dehydration products.

209 **Data Processing and Error Evaluation**

210 By calculating the relative area intensities of the strongest diffraction lines in the
211 XRD patterns, subtracting the background, fitting the area intensities of the strongest
212 diffraction peaks with Gaussian curves, and finally normalizing the area intensity to the
213 intensity of the incident beam and acquisition time, we can obtain the transformation
214 degree and relative mass fraction of each solid phase in the experimental product of the
215 antigorite dehydration reaction (e.g., Perrillat et al., 2005). By adding the normalized
216 intensities of the strongest and most obvious diffraction peak areas, a graph of intensity

217 (*I*) versus time (*t*) can be established for each phase. The relative mass fraction or
218 relative intensity is plotted as a function of time to study its effect on the reaction
219 kinetics.

220 For a dehydration reaction at a given temperature, the degree of departure from
221 the fitted line (with the intercept equivalent to zero) of each data point on the plot of
222 the molar percent of forsterite or talc produced versus that of antigorite decomposed
223 can be considered the uncertainty. In addition, isothermal kinetic model simulations
224 can be used to provide constraints on the error evaluation of decomposed antigorite.
225 Uncertainties in quantitative phase analysis may mainly result from the preferred
226 orientation of phyllosilicate minerals (i.e., antigorite and talc) and the grain
227 morphology and size of the three phases controlled by kinetic mechanisms.

228

229

RESULTS

230 Reaction Progress of Antigorite Dehydration

231 Table 1 shows the conditions and results of thirty-six experiments, in which
232 systematic time-dependent reaction experiments were carried out under the conditions
233 of a confining pressure of 200 MPa and temperatures of 500-650 °C. XRD analysis of
234 all the experimental products showed that only forsterite and talc were produced in our
235 experiments through the following reaction:

236



237 Figure 3 shows a comparison of XRD patterns of dehydrated products over time
238 for representative samples at a confining pressure of 200 MPa and a temperature of
239 600 °C. From the figure, we can see that there is no obvious dehydration of the
240 antigorite when $t \leq 15$ h; thus, the XRD patterns are basically consistent with that of the
241 starting material. After the phase identification of the experimental products, water
242 subtraction and normalization of the solid phases, we find that the samples are not
243 dehydrated for durations of 6 h or less and that the degree of dehydration of the sample
244 after 9 h is very small, with only 3 wt.% talc produced. The dehydration degree is also
245 small for the 15-h sample, in which the amount of talc produced is only 8 wt.% (Table
246 1). With increasing duration, the characteristic peaks of forsterite and talc in the XRD
247 diffraction pattern are increasingly obvious, and the intensity of the peak increases. For
248 instance, the amount of talc produced reached 32 wt.% in a 36-h sample. We also
249 carried out experiments under a confining pressure of 200 MPa at 580 °C, 565 °C,
250 550 °C and 500 °C (Table 1). The maximum durations for operation under these target
251 *PT* conditions were 360 h, 360 h, 6 h, and 745.5 h, respectively. The results show that
252 dehydration of antigorite does not occur at 565 °C but occurs significantly at 580 °C,
253 suggesting that a certain temperature between 565 and 580 °C can be regarded as the
254 temperature stability limit of antigorite under 200 MPa pressure.

255 As clearly shown in Figure 4, with increasing duration, the decomposition of
256 antigorite increases rapidly at first and then slowly; correspondingly, the production of
257 talc and forsterite exhibits similar changes. However, the degrees of decomposition of
258 antigorite and crystallization of talc and forsterite are distinct. Under initially

259 water-unsaturated conditions, the degrees of change in the three phases are more
260 obvious for experiments at 625 and 650 °C (Figures 4b and 4c). Furthermore, the
261 reaction rate at 650 °C is much faster than that at 625 °C, and the reaction rate at
262 625 °C is much faster than that at 600 °C. Accordingly, at 650 °C, the decomposition
263 of antigorite and the crystallization of both forsterite and talc reach near completion
264 within 9 h. In contrast, the reaction progress at 600 °C is ~80% when the duration is up
265 to 84 h and changes very slowly thereafter (Figure 4a), implying that the water activity
266 is close to 1 (i.e., water saturation) beginning at 84 h. The data point scattering reflects
267 the uncertainty in the quantitative phase analysis. Under water-saturated conditions,
268 however, the reaction rate is much slower at 650 °C (Figure 4d).

269 **Kinetic Parameters**

270 In our experiments, antigorite dehydrates to only forsterite + talc + water, and the
271 Avrami model suitable for heterogeneous solid-state reactions (Avrami, 1939) is thus
272 used to simulate the isothermal kinetic data of the experimental products over time at
273 600, 625 and 650 °C. To study the dehydration kinetics, the strongest peak area
274 calculation is performed for all XRD measurements on recovered run products. For
275 instance, for the strongest peak of antigorite, the peak area at a given temperature
276 before the start of the reaction is regarded as the initial intensity I_0 , and the intensity at
277 time t for a given PT condition is marked as I_t ; then, I_t/I_0 represents the relative
278 intensity. For isothermal reactions, the reaction progress α can be expressed as follows:

$$279 \quad \alpha = 1 - \frac{I_t}{I_0} \quad (2)$$

280 where I_t represents the integrated intensity of a peak at time t (e.g., Wang et al., 2015).
281 This reaction progress can be well described by the classic Avrami model, which
282 includes the two processes of nucleation and growth and can be expressed by the
283 following equation:

$$284 \quad \alpha = 1 - \exp(-kt^n) \quad (3)$$

285 where t is the time in seconds, k is the rate constant and n is the Avrami exponent. As
286 the Avrami constants, the parameters k and n are considered to have great importance
287 in indicating the nucleation and crystallization mechanisms. In terms of a combination
288 of nucleation and growth processes, Cahn (1956) derived the theoretical n value in the
289 Avrami equation, which varies from 1 to 4. The k and n values are considered to
290 depend on both the time and dimensionality or morphology of the nucleation and
291 growth processes. For $n=1$, the nucleation rate is faster than the growth rate, and when
292 $n=4$, the growth rate is faster than the nucleation rate.

293 Figure 5 shows the fitting to the experimental data at 600, 625, and 650 °C, and
294 the results are summarized in Table 2. Fitting of the data under initially
295 water-unsaturated conditions yields $n=1.33\pm 0.13$ and $\ln k=-15.92\pm 1.49$ at 600 °C,
296 $n=1.40\pm 0.02$ and $\ln k=-14.83\pm 0.38$ at 625 °C, and $n=1.50\pm 0.02$ and $\ln k=-13.50\pm 0.38$ at
297 650 °C for the decomposition of antigorite (Figure 5a); $n=1.37\pm 0.08$ and
298 $\ln k=-15.84\pm 0.90$ at 600 °C, $n=1.24\pm 0.01$ and $\ln k=-13.21\pm 0.19$ at 625 °C, and
299 $n=1.15\pm 0.01$ and $\ln k=-11.19\pm 1.67$ at 650 °C for the crystallization of forsterite (Figure
300 5b); and $n=2.68\pm 0.20$ and $\ln k=-30.43\pm 2.18$ at 600 °C, $n=2.71\pm 0.05$ and

301 $\ln k = -26.88 \pm 0.89$ at 625 °C, and $n = 2.67 \pm 0.00$ and $\ln k = -24.58 \pm 0.03$ at 650 °C for the
302 crystallization of talc (Figure 5c). Under water-saturated conditions, $n = 1.16 \pm 0.08$ and
303 $\ln k = -13.29 \pm 0.92$ at 650 °C for the decomposition of antigorite (Figure 5d).

304 The reaction rate constant k shown in equation (3) is expressed by the Arrhenius
305 equation:

$$306 \quad k = A \exp(-E/RT) \quad (4)$$

307 where A is the pre-exponential factor, E is the activation energy in kJ/mole, R is the gas
308 constant (8.314 J K/mol), and T is the absolute temperature in K. The fitted line shown
309 in Figure 6 can be obtained by plotting the natural logarithm of the rate constant and
310 the reciprocal of the absolute temperature, which gives the value of E as $353.51 \pm$
311 23.69 kJ/mol. Uncertainty on activation energy is the uncertainty of the slope of the
312 line fit to the data points, and does not include propagated errors from the uncertainty
313 on each data point.

314

315 DISCUSSION

316 The activation energy value obtained in the present study is higher than the two
317 average activation energies (268.1 kJ/mol and 299.2 kJ/mol) obtained by Liu et al.
318 (2019) based on the double Gaussian distribution activation energy model (2-DAEM)
319 but lower than the value (400 kJ/mol) obtained by the same authors using the
320 Flynn–Wall–Ozawa model (Table 3). Furthermore, it is also higher than the activation

321 energy reported by Sawai et al. (2013) and Gualtieri et al. (2012) but lower than the
322 activation energy given by Weber and Greer (1965) (Table 3). However, Gualtieri et al.
323 (2012) concluded that the activation energy of their sample was much lower than that
324 reported by Weber and Greer (1965) because their sample consisted of only ~79 wt.%
325 antigorite. They speculated that if ~21 wt.% of impurities, i.e., chrysotile, which is one
326 of the main low-temperature serpentine minerals, were removed, the activation energy
327 of the sample consisting of 100% antigorite would be approximately 322 kJ/mol
328 (Gualtieri et al., 2012), which is very close to the value of 353.51 ± 23.69 kJ/mol that
329 we obtained for the nearly pure antigorite sample. As the pre-exponential factor is
330 linearly correlated with the activation energy, the difference in activation energy may
331 result from a large change in the absolute value of the activation energy caused by the
332 pre-exponential factor (Liu et al., 2019). According to equation (4), this difference in
333 activation energy can be used to reflect the change in the reaction rate (kinetic). Thus,
334 the factors (such as particle size, modulation structure, etc.) affecting dehydration
335 kinetics can be considered to have an effect on the activation energy. In addition,
336 chemical and structural differences in the starting material of antigorite (Wunder et al.,
337 1997, 2001) and water activity (Perrillat et al., 2005) may possibly result in slightly
338 different *PT* locations and invariant points for the serpentine dehydration reaction (e.g.,
339 Ulmer and Trommsdorff, 1995; Wunder and Schreyer, 1997; Figure 7).

340 **Effect Factors for Dehydration Kinetics and Phase Stability**

341 Several high-*PT* experimental studies (Bose and Ganguly, 1995; Bromiley and

342 Pawley, 2003; Ulmer and Trommsdorff, 1995; Wunder and Schreyer, 1997) and field
343 observations of eclogite-facies rocks (Auzende et al., 2002; Guillot et al., 2000;
344 Scambelluri et al., 1995) have shown that antigorite is the only serpentine variety that
345 can exist stably under mantle conditions. Additionally, antigorite follows reaction (1) at
346 high temperatures of 600-700 °C and pressures lower than ~2 GPa (Figure 7; Ulmer
347 and Trommsdorff, 1995). Our experiments were performed at a constant pressure of
348 200 MPa, and the XRD analyses of the products indicated that only forsterite and talc
349 were produced in addition to water, which is consistent with the results of previous
350 studies (e.g., Evans et al., 1976; Ulmer and Trommsdorff, 1995; Wunder and Schreyer,
351 1997; Figure 7). As illustrated in Figure 7, our data show that the dehydration
352 temperature (~570 °C) of our antigorite ($m=15$) is slightly higher than the reaction
353 boundaries (~540±10 °C) at 200 MPa delineated based on the data of Evans et al.
354 (1976) and Wunder and Schreyer (1997), which may be due to the lower m value of
355 our samples than theirs ($m=17$). This is also one of the main reasons that our sample
356 has a higher stability and activation energy than the antigorite used in previous
357 dehydration kinetics studies (e.g., Liu et al., 2019; Sawai et al., 2013) (Table 3),
358 because for dehydration reaction at the same temperature, a lower dehydration
359 temperature (higher m value) will result in a faster reaction rate and a corresponding
360 lower activation energy. For similar m values, the dehydration temperature of our
361 sample and that of a natural sample from Cerro del Almirez, Spain (Padrón-Navarta et
362 al., 2008), at different pressures can be used to delineate a reaction boundary, which
363 has a trend similar to those of the reaction boundaries determined by Evans et al. (1976)

364 and Wunder and Schreyer (1997).

365 Previous studies suggested that if the system contains a small amount of
366 aluminum, the entire phase boundary will migrate to a higher temperature by
367 ~50-100 °C (e.g., Bromiley and Pawley, 2003). However, our antigorite contains only
368 0.06 wt.% Al₂O₃, which is much lower than the aluminum contents of the samples used
369 previously [e.g., 3.45 wt.% in Perrillat et al. (2005) and Chollet et al. (2011); 1.51
370 wt.% in Inoue et al. (2009); 1.73 wt.% in Sawai et al. (2013); and 1.03 wt.% in Liu et
371 al. (2019)]. In contrast, the effect of iron on the thermal stability of antigorite is
372 twofold. On the one hand, Fe²⁺ is known to reduce its stability by ~15-20 °C (Ulmer
373 and Trommsdorff, 1999); on the other hand, Fe³⁺, like Al and Cr, could stabilize
374 antigorite to higher *PT* conditions (e.g., Bromiley and Pawley, 2003; Debret et al.,
375 2015; Padrón-Navarta et al., 2008, 2013). Recently, 10 wt.% FeO was determined to
376 decrease the stability of antigorite by only 25 °C (Merkulova et al., 2016), suggesting
377 that the effect of iron is subordinate to that of Al. The amount of iron contained in our
378 sample is 0.97 wt.% TFeO; thus, the effect of low iron and aluminum contents on the
379 phase boundary of antigorite might be partially offset.

380 The sample powders used in this study (~10-15 μm) are slightly larger than those
381 in some previous experiments [e.g., 5-10 μm in Liu et al. (2019) and 2-3 μm in
382 Perrillat et al. (2005)]. This may be not only another main reason why our sample
383 dehydration temperature is slightly higher than theirs within a certain time frame (e.g.,
384 Llana-Funez et al., 2007) but also one of the main reasons for the higher activation
385 energy of our coarse-grained samples than those of the fine-grained samples used in

386 previous studies (Liu et al., 2019; Perrillat et al., 2005) (Table 3). The effect of grain
387 size on dehydration kinetics can also be reflected by the differences in activation
388 energy of various grain sizes, as the lower the activation energy is, the faster the
389 reaction rate is. For example, earlier experiments on the dehydration kinetics of
390 trehalose dihydrate performed by Taylor and York (1998) suggested that the activation
391 energy decreases with decreasing particle size because smaller particles contain more
392 lattice defects, allowing water to be released more easily, and thus have lower
393 activation energy. Similar results were also reflected in the study of lizardite
394 dehydration kinetics by Llana-Fúnez et al. (2007), who determined average activation
395 energies of 429 ± 201 and 528 ± 34 kJ/mol for powdered and intact samples, respectively.
396 Correspondingly, the dehydration rate of powdered samples is 10 times faster than that
397 of intact samples under the same conditions (Llana-Fúnez et al., 2007). Concurrently,
398 Candela et al. (2007) studied the dehydration kinetics of chrysotile at low pressure and
399 found that fine particles with large surface-to-volume ratios dehydrated more rapidly
400 than larger particles. In this regard, the dehydration kinetics of antigorite were
401 proposed to be dominated by the diffusion of hydrogen in the mineral. If this is correct,
402 the kinetics could be a function of the diffusion length of hydrogen, which is
403 proportional to the specific surface of the grains or the square of the inverse of the
404 grain size (Sawai et al., 2013). Thus, doubling the grain size results in four-times
405 slower kinetics. In addition, the diffusion coefficient of hydrogen in the mineral should
406 depend on temperature, probably with an Arrhenius relation, and thus may be a source
407 of the temperature dependence of the dehydration kinetics of antigorite (Sawai et al.,

408 2013). Recently, Wang et al. (2015) conducted an experimental study on the
409 dehydration kinetics of natural talc and found that the dehydration rate of talc
410 increased with decreasing particle size, but when the particle size was less than 5 μm ,
411 there was almost no effect on the dehydration rate. Therefore, fine-grained antigorite is
412 generally more likely to dehydrate, and the dehydration rate may be faster than that of
413 a coarse-grained sample.

414 In addition, water activity is an important factor affecting the dehydration
415 boundary of antigorite. Previous studies have shown that the stability limit of antigorite
416 (i.e., the highest temperature under water-saturated conditions) shifts toward lower
417 temperatures with decreasing water activity (e.g., Perrillat et al., 2005; Hilairet et al.,
418 2006; Figure 7). As shown in Table 1 and Figure 4d, the water-saturated samples
419 (Atg60 and Atg61) do not completely decompose to form forsterite + talc at longer
420 durations, but the initially water-unsaturated sample Atg23 under the same *PT*
421 conditions does nearly completely decompose. The powdered samples Atg60 and
422 Atg61 are immersed in water so that the voids within the sample powders are filled
423 with water to form a water-saturated environment, which is supported by the presence
424 of free water in the recovered sample (e.g., Perrillat et al., 2005). In contrast, the voids
425 within sample Atg23 are partially filled with water generated only by the
426 decomposition of the sample itself, the water activity of the sample increases with
427 duration, and the sample becomes water saturated until near completion of the
428 dehydration reaction. Furthermore, we find that the rate of dehydration slows down
429 significantly when the sample is heated at 600 °C for 60-120 h (Figure 4a), which

430 means that the water activity of the sample increases, making it impossible for our
431 antigorite to completely dehydrate at this temperature. At higher temperatures (625 and
432 650 °C), however, the rate of dehydration decreases significantly when the sample is
433 nearly completely decomposed in much shorter durations (Figures 4b and 4d). This
434 response implies that an increase in temperature can offset the effect of an increase in
435 water activity.

436 In summary, combining our results with those of previous studies, the stability of
437 antigorite is affected by the modulation structure (i.e., m value), aluminum content,
438 iron content, water activity, and deformation within the Earth. Antigorites with low m
439 values can be stabilized at higher temperatures. An increase in aluminum or Fe^{3+}
440 content can cause the stable boundary to move toward higher temperatures, while an
441 increase in Fe^{2+} content has the opposite and smaller effect. Water activity acts as the
442 driver of the reaction and determines the stability of the antigorite under certain PT
443 conditions (e.g., Perrillat et al., 2005). Different from our static experiments,
444 differential stress must be present within the earth where deformation geometry (such
445 as compression, shear, or the direction of the foliation plane with respect to the
446 maximum principal stress) may change the phase stability of antigorite and thus its
447 dehydration kinetics (Okazaki and Katayama, 2015; Shao et al., 2021; Takahashi et al.,
448 2011). A reduction in particle size can increase the reaction rate (Candela et al., 2007;
449 Llana-Funez et al., 2007; Taylor and York, 1998).

450 **Kinetic Mechanism**

451 For the decomposition of antigorite, higher n values are found at high
452 temperatures than at low temperatures (Figure 5 and Table 2). The mean n value for
453 antigorite decomposition at the three examined temperatures is 1.41 ± 0.09 , indicating
454 an instantaneous nucleation mechanism followed by a growth process governed by
455 chemical species diffusing to the crystal surface (Christian, 1975). Such a mechanism
456 was reported by Perrillat et al. (2005) for the crystallization of forsterite and talc-like
457 phases in the process of antigorite dehydration. The n value ($n=1.37$) for the
458 crystallization of forsterite is close to that ($n=1.33$) for the decomposition of antigorite
459 at 600 °C in the same reaction process. However, the value of n for the crystallization
460 of forsterite decreases to 1.15 when the temperature increases to 650 °C (Figure 5),
461 indicating that the crystallization of forsterite is mainly controlled by the growth
462 process with increasing temperature and is accompanied by rapid nucleation saturation.
463 In contrast, the crystallization of talc shows little change in the n value at 600, 625 and
464 650 °C (average $n=2.69 \pm 0.02$), suggesting that the formation mechanism of talc is the
465 same at the three temperatures and is dominated by nucleation. In other words, the
466 nucleation rate of forsterite becomes quite high with increasing temperature, while at
467 the initial stage of the reaction, the nucleation of talc is no longer instantaneous but
468 slow and then increases with time. In addition, the k values of the three minerals
469 increase with increasing temperature, which is similar to the results of a study on talc
470 dehydration kinetics (Wang et al., 2015). Using various methods, however, previous
471 studies determined different kinetic mechanisms for antigorite dehydration. Based on
472 XRD, for example, Perrillat et al. (2005) obtained $n=2$ for the dehydration of antigorite,

473 indicating a mechanism of surface growth at the grain edge. In contrast, also using
474 XRD, Gualtieri et al. (2012) found that antigorite dehydration is controlled by a
475 one-dimensional diffusion process, which is similar to the finding obtained by Sawai et
476 al. (2013) using in situ high-temperature infrared spectroscopy analysis. In terms of
477 thermogravimetric analysis and in situ XRD, Balucan et al. (2011) found that the
478 dehydration kinetics of antigorite can be well modeled by a three-dimensional phase
479 boundary reaction model. Most recently, also employing thermogravimetric analysis,
480 Liu et al. (2019) determined that the antigorite dehydration kinetics follow 2-DAEM.
481 However, most of these studies did not perform microstructural observations of
482 products to support their analyses of the kinetic mechanism of antigorite dehydration.

483 To confirm our kinetic results, we conducted two complementary experiments
484 (Atg103 and Atg112) and further analysis of the run products. Figure 8 shows
485 backscattered electron (BSE) images of the recovered products produced at 600 and
486 650 °C. Under 600 °C and initially water-unsaturated conditions, the experiment
487 conducted for 48 h generated abundant fine grains of forsterite (Figure 8a), suggesting
488 that the formation of forsterite is controlled by the growth process, followed by rapid
489 nucleation saturation. Furthermore, large crystals of talc were generated in this
490 experiment, indicating that the formation of talc is mainly controlled by nucleation.
491 These observations based on the BSE images of the recovered samples were consistent
492 with the kinetic results that $n \sim 1.3$ for the formation of forsterite and ~ 2.7 for the
493 formation of talc. Under 650 °C and water-saturated conditions, in contrast, the
494 amounts of forsterite and talc produced were much lower in the experiment conducted

495 for only 3 h (Figure 8b), which is basically consistent with the results of the powder
496 XRD analyses.

497 **Isothermal Kinetic Model and Fluid Production Rates**

498 Previous studies have shown that the hypocenters of the lower-plane seismicity in
499 a DSZ are roughly distributed along the estimated location of the 600-650 °C
500 isotherms (e.g., Peacock, 2001). According to the abovementioned dehydration kinetics
501 data of antigorite at 600 and 650 °C, we can calculate the fluid production rate during
502 the antigorite dehydration process at the two endmember temperatures corresponding
503 to the isotherms bounding the hypocenters. On the basis of the fitting to the
504 decomposition of antigorite at the two temperatures, as shown in Figures 5a and 5d, we
505 can obtain the following relationships indicating the variation in the progress of the
506 dehydration reaction with time at 600 and 650 °C:

$$507 \quad \alpha(T = 600 \text{ °C and initially water-unsaturated}) = 1 - \exp\left(-\frac{t^{1.33 \pm 0.13}}{8178342.01 \pm 0.23}\right) \quad (5)$$

$$508 \quad \alpha(T = 650 \text{ °C and initially water-unsaturated}) = 1 - \exp\left(-\frac{t^{1.50 \pm 0.02}}{716404.33 \pm 0.68}\right) \quad (6)$$

$$509 \quad \alpha(T = 650 \text{ °C and water-saturated}) = 1 - \exp\left(-\frac{t^{1.16 \pm 0.08}}{588893.13 \pm 0.40}\right) \quad (7)$$

510 Figure 9 shows the curves indicating variations in the progress of the reaction
511 with time at 600 and 650 °C calculated according to the above three equations. Some
512 data points at 600 °C seriously depart from the curve because these data have large
513 errors and thus were not included in fitting to obtain n and k used for modelling the

514 curve. Despite the large errors of some data points, most of the data are consistent with
515 the simulated dehydration kinetics curve. The rate of antigorite dehydration clearly
516 increases with increasing temperature under initially water-unsaturated conditions. At
517 $t=800$ min, for instance, the antigorite dehydration progress is only ~18.96% at 600 °C
518 and almost 100% at 650 °C under initially water-unsaturated conditions, while it is
519 only ~37.96% at 650 °C under water-saturated conditions. When half of the antigorite
520 is consumed during the breakdown reaction, the dehydration rate can be obtained
521 according to the half-life of the reaction (e.g., Chollet et al., 2011),

$$522 \quad V_{1/2} = \frac{C_{\text{H}_2\text{O}}}{t_{1/2}} \times \frac{\rho}{\rho_{\text{H}_2\text{O}}} \quad (8)$$

523 where $t_{1/2}$ is the half-life of the reaction when the reaction progress is 50% and $C_{\text{H}_2\text{O}}$
524 represents the water content of the mineral. ρ and $\rho_{\text{H}_2\text{O}}$ are the densities of the
525 mineral and water, respectively. In this study, antigorite has a density of 2.593 g/cm³
526 and a water content of ~12.19 wt.%. At a pressure of 1.5 GPa, the water density is
527 ~1.057, ~1.048, and ~1.038 g/cm³ at 600, 625, and 650 °C, respectively (Zhang and
528 Duan, 2005). As shown in Figure 9, the half-lives of the antigorite dehydration reaction
529 at 600, 625 and 650 °C under initially water-unsaturated conditions are 32.65, 8.48 and
530 1.77 h, respectively. In contrast, the half-life of antigorite breakdown at 650 °C under
531 water-saturated conditions is 18.37 h. Therefore, the calculated fluid production rates
532 in the process of antigorite dehydration at 600, 625, and 650 °C under initially
533 water-unsaturated conditions are 2.54×10^{-6} , 9.80×10^{-6} , and $4.69 \times 10^{-5} \text{ m}_{\text{fluid}}^3 \text{ m}_{\text{rock}}^{-3} \text{ s}^{-1}$,
534 respectively. Under initially water-saturated conditions, the calculated fluid production

535 rate is $4.52 \times 10^{-6} \text{ m}_{\text{fluid}}^3 \text{ m}_{\text{rock}}^{-3} \text{ s}^{-1}$ at 650 °C, which is ~10 times slower than that under
536 initially water-unsaturated conditions at the same temperature, similar to the result of
537 Perrillat et al. (2005). These values are comparable to those reported previously for
538 antigorite dehydration [$3 \times 10^{-5} - 3 \times 10^{-4} \text{ m}_{\text{fluid}}^3 \text{ m}_{\text{rock}}^{-3} \text{ s}^{-1}$ at 625-700 °C in Sawai et al.
539 (2013), $8 \times 10^{-5} \text{ m}_{\text{fluid}}^3 \text{ m}_{\text{rock}}^{-3} \text{ s}^{-1}$ at 620 °C and $4.4 \times 10^{-4} \text{ m}_{\text{fluid}}^3 \text{ m}_{\text{rock}}^{-3} \text{ s}^{-1}$ at 660 °C in Liu et
540 al. (2019), $10^{-4} \text{ m}_{\text{fluid}}^3 \text{ m}_{\text{rock}}^{-3} \text{ s}^{-1}$ in Chollet et al. (2011), and $3 \times 10^{-8} - 3 \times 10^{-6}$
541 $\text{m}_{\text{fluid}}^3 \text{ m}_{\text{rock}}^{-3} \text{ s}^{-1}$ in Perrillat et al. (2005)]. Likewise, the rate at which antigorite
542 dehydration releases fluids in this study is far greater than the viscous relaxation rate of
543 antigorite ($3.0 \times 10^{-12} - 3.0 \times 10^{-7} \text{ s}^{-1}$, i.e., the reciprocal of Maxwell's relaxation time)
544 under subduction zone conditions reported by Hilairet et al. (2007). Previous studies
545 have shown that pressure has no obvious effect on the dehydration kinetics of
546 antigorite (e.g., Perrillat et al., 2005; Rubie and Thompson, 1985). Thus, the fluid
547 production rate calculated above can be applied to shallow intermediate-depth
548 earthquake layers in hot subduction zones (e.g., Kii, Tokai, and Cascadia), where
549 antigorite breakdown into forsterite + talc + water is possible (Figure 7).

550

IMPLICATIONS

551 For decades, intermediate-depth earthquakes have commonly been considered to
552 result from the dehydration of antigorite (e.g., Chollet et al., 2011; Ferrand et al., 2017;
553 Hilairet et al., 2017; Liu et al., 2019; Miller et al., 2003; Raleigh and Paterson, 1965;
554 Reynard, 2013; Sawai et al., 2013). In their pioneering work on dehydration
555 embrittlement, Raleigh and Paterson (1965) deformed natural serpentinites which

556 contained other phases such as olivine, and explained that embrittlement occurred
557 within the dehydrating antigorite due to fluid overpressure. However, many later
558 experiments have indicated that embrittlement occurs in adjacent more brittle
559 peridotite or the piston, rather than in the dehydrating antigorite itself (e.g., Dobson et
560 al., 2002; Ferrand et al., 2017; Jung et al., 2004; Xia, 2013). In fact, antigorite shows
561 semibrittle behavior under mantle conditions and no dehydration embrittlement occurs
562 (e.g., Chernak and Hirth, 2011; Gasc et al., 2011; Shao et al., 2021). In lithospheric
563 mantle, only partial serpentinization (17-31%) occurs (Garth and Rietbrock, 2014) and
564 the distribution of serpentine is heterogeneous (Dunkel et al., 2017). Some researchers
565 have proposed that the fluid produced by antigorite dehydration at intermediate depths
566 in a subduction zone likely migrates into the surrounding brittle peridotite region
567 (Barcheck et al., 2012; Rutter et al., 2009) so as to generate not only high pore fluid
568 pressure but also instantaneous over stress due to the lateral transfer of the stress
569 previously supported by the dehydrating antigorite, thereby inducing earthquakes. This
570 inference is partially similar to the sudden stress transfer model proposed by Ferrand et
571 al. (2017), but it is probably true at $P < 2$ GPa. Whether or not the embrittlement of
572 peridotite around the dehydrating antigorite occurs was considered to depend on the
573 competition between the rate of fluid production and migration into the peridotite and
574 the deformation rate of the peridotite (e.g., Chollet et al., 2011; Liu et al., 2019;
575 Perrillat et al., 2005). In the case when fluid migration from dehydrating antigorite to
576 adjacent peridotite is negligible, if fluid is produced at a faster rate than deformation, a
577 seismic rupture may be nucleated. However, several studies have shown that fast

578 dehydration kinetics may not lead to dehydration embrittlement (e.g., Chernak and
579 Hirth, 2011; Gasc et al., 2011).

580 Under the conditions of syndeformational antigorite dehydration reaction, there
581 must be another heterogeneous system, namely, antigorite and its dehydration products
582 (e.g., Takahashi et al., 2011). As stated by Gasc et al. (2011), we should emphasize the
583 role of reaction products whose size is in turn controlled by reaction kinetics (Rutter
584 and Brodie, 1988). In a recent study by Proctor and Hirth (2015), forsterite produced
585 by the dehydration of antigorite has a finer grain size in drained samples than in
586 undrained samples. This means that in the interior of the earth, the dehydration of
587 antigorite may produce finer-grained forsterite ($<1 \mu\text{m}$) than that observed in our
588 undrained experiments (Figure 8). Such fine-grained forsterites may facilitate faulting
589 by their superplasticity (Rutter and Brodie, 1988; Schubnel et al., 2013). However,
590 several studies suggest that stick-slip occurs under the conditions where dehydration of
591 antigorite happens (Okazaki and Katayama, 2015; Takahashi et al., 2011). SEM
592 observations also indicate heterogeneous dehydration products (Takahashi et al., 2011),
593 in which forsterite displays velocity weakening (Boettcher et al., 2007; King and
594 Marone, 2012) while antigorite shows velocity strengthening and thus inhibits normal
595 stick-slip behavior (Chernak and Hirth, 2011; Shao et al., 2021). Consequently, when
596 significant dehydration occurs in the core of a serpentinized fault zone at $650 \text{ }^\circ\text{C}$,
597 normal stick-slip behavior can be expected as the velocity-weakening behavior of
598 forsterite dominates the frictional properties of the entire fault gouge (Boettcher et al.,
599 2007; King and Marone, 2012; Okazaki and Katayama, 2015). Once triggered, an

600 earthquake will propagate into the more brittle surrounding rocks. At 600 °C, slow
601 stick-slip could be induced by interaction between the velocity strengthening behavior
602 of antigorite and the velocity-weakening behavior of forsterite (Okazaki and Katayama,
603 2015). In addition, unstable slip can also be induced by water or talc because such
604 phases may reduce the rate dependence of antigorite (e.g., Moore and Lockner, 2011;
605 Okazaki and Katayama, 2015), thereby facilitating faulting. In a heterogeneous system,
606 the sizes of the dehydration products are crucial, which in turn depend on the kinetic
607 mechanism of dehydration. In this study, the reaction of antigorite dehydration to
608 fine-grained forsterite and large talc crystals is controlled by a heterogeneous
609 nucleation and growth mechanism. As the temperature increases from 600 to 650 °C,
610 the influence of forsterite by growth control increases (n decreases to close to 1, Figure
611 5b), resulting in the formation of finer-grained forsterite. This change indicates that the
612 increase in the dehydration degree in the core of a serpentinized fault zone will
613 facilitate faulting, triggering earthquakes and extending to the more brittle peridotite.
614 Therefore, the reaction of antigorite dehydration to talc, one of the weakest
615 phyllosilicates (Moore and Lockner, 2011), and fine-grained forsterite may be
616 responsible for shallow intermediate-depth seismicity in hot subduction zones (Figure
617 7).

618

619

FUNDING

620 This work was supported by the Strategic Priority Research Program (B) of the
621 Chinese Academy of Sciences (Grant Nos. XDB42020403 and XDB18000000), the

622 National Natural Science Foundation of China (Grant No. 41702224), a research grant
623 from the State Key Laboratory of Earthquake Dynamics (Grant No. LED2017B06),
624 and the Pearl River Talent Plan of Guangdong Province. This is a contribution to No.
625 IS-XXXX from GIGCAS.

626

627

ACKNOWLEDGMENTS

628 We thank Tingting Shen for the helpful discussion and guidance during TEM
629 measurement of the modulation structure of antigorite. We also appreciate the valuable
630 comments and suggestions from the two anonymous reviewers and the Associate
631 Editor, Sarah Brownlee, which helped us improve the manuscript.

632

633

REFERENCES CITED

- 634 Abers, G.A., Nakajima, J., van Keken, P.E., Kita, S., and Hacker, B.R. (2013)
635 Thermal-petrological controls on the location of earthquakes within subducting
636 plates. *Earth and Planetary Science Letters*, 369-370, 178-187.
- 637 Arkwright, J., Rutter, E., Brodie, K., and Llana-Fúnez, S. (2008) Role of porosity and
638 dehydration reaction on the deformation of hot-pressed serpentinite aggregates.
639 *Journal of the Geological Society*, 165, 639-649.
- 640 Auzende, A.-L., Devouard, B., Guillot, S., Daniel, I., Baronnet, A., and Lardeaux, J.-M.
641 (2002) Serpentinites from Central Cuba: petrology and HRTEM study. *European*
642 *Journal of Mineralogy*, 14, 905-914.
- 643 Avrami, M. (1939) Kinetics of phase change. *Journal of Chemical Physics*, 7,

- 644 1103-1112.
- 645 Balucan, R.D., Kennedy, E.M., Mackie, J.F., and Dlugogorski, B.Z. (2011)
646 Optimization of antigorite heat pre-treatment via kinetic modeling of the
647 dihydroxylation reaction for CO₂ mineralization. *Greenhouse Gases-Science and*
648 *Technology*, 1(4), 294-304.
- 649 Barcheck, C.G, Wiens, D.A., van Keken, P.E., and Hacker, B.R. (2012) The
650 relationship of intermediate- and deep-focus seismicity to the hydration and
651 dehydration of subducting slabs. *Earth and Planetary Science Letters*, 349-350,
652 153-160.
- 653 Bose, K., and Ganguly, J. (1995) Experimental and theoretical studies of the stabilities
654 of talc, antigorite and phase A at high pressures with applications to subduction
655 processes. *Earth and Planetary Science Letters*, 136, 109-121.
- 656 Brasse, H., Kapinos, G., Mutschard, L., Alvarado, G. E., Worzewski, T., and Jegen, M.
657 (2009) Deep electrical resistivity structure of northwestern Costa Rica.
658 *Geophysical Research Letters*, 36, L02310, doi:10.1029/2008GL036397.
- 659 Bromiley, G.D., and Pawley, A.R. (2003) The stability of antigorite in the system
660 MgO-SiO₂-H₂O (MSH) and MgO-Al₂O₃-SiO₂-H₂O (MASH): the effects of Al³⁺
661 substitution on high-pressure stability. *American Mineralogist*, 88, 99-108.
- 662 Brudzinski, M.R., Thurber, C.H., Hacker, B.R., and Engdahl, E.R. (2007) Global
663 prevalence of double Benioff zones. *Science*, 316, 1472-1474.
- 664 Cahn, J.W. (1956) The kinetics of grain boundary nucleated reactions. *Acta*
665 *Metallurgica*, 4, 449-459.

- 666 Candela, P.A., Crummett, C.D., Earnest, D.J., Frank, M.R., and Wylie, A.G. (2007)
667 Low-pressure decomposition of chrysotile as a function of time and temperature.
668 American Mineralogist, 92, 1704-1713.
- 669 Cattaneo, A., Gualtieri, A.F., and Artioli, G. (2003) Kinetic study of the
670 dihydroxylation of chrysotile asbestos with temperature by in situ XRPD. Phys.
671 Chem. Minerals, 30, 177-183.
- 672 Chernak, L.J., and Hirth, G. (2010) Deformation of antigorite serpentinite at high
673 temperature and pressure. Earth and Planetary Science Letters, 296(1), 23-33.
- 674 Chernak, L.J., and Hirth, G. (2011) Syndeformational antigorite dehydration produces
675 stable fault slip. Geology, 39(9), 847-850.
- 676 Chollet, M., Daniel, I., Koga, K.T., Morard, G., and Moortele, B. (2011) Kinetics and
677 mechanism of antigorite dehydration: implications for subduction zone seismicity.
678 Journal of Geophysical Research, 116, doi:10.1029/2010JB007739.
- 679 Christian, J.W. (1975). Transformations in Metals and Alloys. Pergamon, New York.
- 680 Debret, B., Bolfan-Casanova, N., Padrón-Navarta, J.A., Martin-Hernandez, F.,
681 Andreani, M., Garrido, C.J., López Sánchez-Vizcaíno, V., Gómez-Pugnaire, M.T.,
682 Muñoz, M., and Trcera, N. (2015) Redox state of iron during high-pressure
683 serpentinite dehydration. Contributions to Mineralogy and Petrology, 169, doi:
684 [10.1007/s00410-015-1130-y](https://doi.org/10.1007/s00410-015-1130-y).
- 685 Dobson, D.P., Meredith, P.G., and Boon, S.A. (2002) Simulation of subduction zone
686 seismicity by dehydration of serpentine. Science, 298(5597), 1407-1410.
- 687 Dunkel, K.G., Austrheim, H., Renard, F., Cordonnier, B., and Jamtveit, B. (2017)

- 688 Localized slip controlled by dehydration embrittlement of partly serpentinized
689 dunites, Leka Ophiolite complex, Norway. *Earth and Planetary Science Letters*,
690 463, 277-285.
- 691 Eggler, D.H., and Ehmann, A.N. (2010) Rate of antigorite dehydration at 2 GPa
692 applied to subduction zones. *American Mineralogist*, 95, 761-769.
- 693 Evans, B.W., Johannes, W., Oterdoom, H., and Trommsdorff, V. (1976) Stability of
694 chrysotile and antigorite in the serpentinite multisystem. *Schweizerische*
695 *Mineralogische und Petrographische Mitteilungen*, 56, 79-93.
- 696 Evans, R.L., Wannamaker, P.E., McGary, R.S., and Elsenbeck, J. (2014) Electrical
697 structure of the central Cascadia subduction zone: The EMSLAB Lincoln Line
698 revisited. *Earth and Planetary Science Letters*, 402, 265-274.
- 699 Ferrand, T.P. (2019) Seismicity and mineral destabilizations in the subducting mantle
700 up to 6 GPa, 200 km depth. *Lithos*, 334-335, 205-230.
- 701 Ferrand, T.P., Hilairat, N., Incel, S., Deldicque, D., Labrousse, L., Gasc, J., Renner, J.,
702 Wang, Y., Green, H.W.II, and Schubnel, A. (2017) Dehydration-driven stress
703 transfer triggers intermediate-depth earthquakes. *Nature Communications*, 8, 15247,
704 <https://doi.org/10.1038/ncomms15247>.
- 705 French, M.E., Hirth, G., and Okazaki, K. (2019) Fracture-induced pore fluid pressure
706 weakening and dehydration of serpentinite. *Tectonophysics*, 767, 228168,
707 doi:10.1016/j.tecto.2019.228168.
- 708 Garth, T., and Rietbrock, A. (2014) Order of magnitude increase in subducted H₂O
709 due to hydrated normal faults within the Wadati-Benioff zone. *Geology*, 42,

- 710 207-210.
- 711 Gasc, J., Hilairret, N., Yu, T., Ferrand, T., Schubnel, A., and Wang, Y. (2017) Faulting of
712 natural serpentinite: Implications for intermediate-depth seismicity. Earth and
713 Planetary Science Letters, 474, 138-147.
- 714 Gasc, J., Schubnel, A., Brunet, F., Guillon, S., Mueller, H.-J., and Lathe, C. (2011)
715 Simultaneous acoustic emissions monitoring and synchrotron X-ray diffraction at
716 high pressure and temperature: Calibration and application to serpentinite
717 dehydration. Physics of the Earth and Planetary Interiors, 189(3), 121-133.
- 718 Gualtieri, A.F., Giacobbe, C., and Viti, C. (2012) The dihydroxylation of serpentine
719 group minerals. American Mineralogist, 97, 666-680.
- 720 Guillot, S., Hattori, K.H., and de Sigoyer, J. (2000) Mantle wedge serpentinization and
721 exhumation of eclogites insights from eastern Ladakh, northwest Himalaya.
722 Geology, 28, 199-202.
- 723 Hacker, B.R., Abers, G.A., and Peacock, S.M. (2003a) Subduction factory 1.
724 Theoretical mineralogy, densities, seismic wave speeds, and H₂O contents. Journal
725 of Geophysical Research, 108(B1), 2029, doi:10.1029/2001JB001127.
- 726 Hacker, B.R., Peacock, S.M., Abers, G.A., and Holloway, S.D. (2003b) Subduction
727 factory 2. Are intermediate-depth earthquakes in subducting slabs linked to
728 metamorphic dehydration reactions? Journal of Geophysical Research, 108(B1),
729 2030, doi:10.1029/2001jb001129.
- 730 Hasegawa, A., Umino, N., and Takagi, A. (1978) Double-plane structure of the deep
731 seismic zone in the northeastern Japan arc. Tectonophysics, 47(1), 43-58.

- 732 Hattori, K.H., and Guillot, S. (2003) Volcanic fronts form as a consequence of
733 serpentinite dehydration in the forearc mantle wedge. *Geology*, 31, 525-528.
- 734 Heinrich, B., and Diane, E. (2008) Electrical conductivity beneath the Bolivian
735 Orocline and its relation to subduction processes at the South American continental
736 margin. *Journal of Geophysical Research*, 113, B07109,
737 doi:10.1029/2007JB005142.
- 738 Hess, H.H., Smith, R.J., and Dengo, G. (1952) Antigorite from the vicinity of Caracas,
739 Venezuela. *American Mineralogist*, 37(1-2), 68-75.
- 740 Hilairet, N., Daniel, I., and Reynard, B. (2006) Equation of state of antigorite, stability
741 field of serpentines, and seismicity in subduction zones. *Geophysical Research*
742 *Letters*, 33, L02302, doi:10.1029/2005GL024728.
- 743 Hilairet, N., Reynard, B., Wang, Y., Daniel, I., Merkel, S., Nishiyama, N., and
744 Petitgirard, S. (2007) High-pressure creep of serpentine, interseismic deformation,
745 and initiation of subduction. *Science*, 318, 1910-1913.
- 746 Huang, R.F., Lin, C.-T., Sun, W.D., Ding, X., Zhan, W.H., and Zhu, J.H. (2017) The
747 production of iron oxide during peridotite serpentinization: Influence of pyroxene.
748 *Geoscience Frontiers*, 8, 1311-1321.
- 749 Hushur, A., Manghnani, M.H., Smyth, J.R., Nestola, F., and Frost, D.J. (2009) Crystal
750 chemistry of hydrous forsterite and its vibrational properties up to 41 GPa.
751 *American Mineralogist*, 94, 751-760.
- 752 Hyndman, R.D., and Peacock, S.M. (2003) Serpentinization of the forearc mantle.
753 *Earth and Planetary Science Letters*, 212(3), 417-432.

- 754 Incel, S., Hilairret, N., Labrousse, L., John, T., Deldicque, D., Ferrand, T., Wang, Y.,
755 Renner, J., Morales, L., and Schubnel, A. (2017) Laboratory earthquakes triggered
756 during eclogitization of lawsonite-bearing blueschist. *Earth and Planetary Science*
757 *Letters*, 459, 320-331.
- 758 Inoue, T., Yoshimi, I., Yamada, A., and Kikegawa, T. (2009) Time-resolved X-ray
759 diffraction analysis of the experimental dehydration of serpentine at high pressure.
760 *Journal of Mineralogical and Petrological Sciences*, 104, 105-109.
- 761 Jung, H., Green, H.W.II, and Dobrzhinetskaya, L.F. (2004) Intermediate-depth
762 earthquake faulting by dehydration embrittlement with negative volume change.
763 *Nature*, 428, 545-549.
- 764 Kelemen, P.B., and Hirth, G. (2007) A periodic shear-heating mechanism for
765 intermediate-depth earthquakes in the mantle. *Nature*, 446, 787-790.
- 766 Liu, T., Wang, D.J., Shen, K.W., Liu, C.J., and Yi, L. (2019) Kinetics of antigorite
767 dehydration: Rapid dehydration as a trigger for lower-plane seismicity in
768 subduction zones. *American Mineralogist*, 104, 282-290.
- 769 Llana-Fúnez, S., Brodie, K.H., Rutter, E.H., and Arkwright, J.C. (2007) Experimental
770 dehydration kinetics of serpentinite using pore volumetry. *Journal of*
771 *Metamorphic Geology*, 25, 423-438.
- 772 Merkulova, M., Munoz, M., Vidal, O., and Brunet, F. (2016) Role of iron content on
773 serpentinite dehydration depth in subduction zones: Experiments and
774 thermodynamic modeling. *Lithos*, 264, 441-452.
- 775 Mishra, O.P., and Zhao, D. (2004) Seismic evidence for dehydration embrittlement of

- 776 the subducting Pacific plate. *Geophysical Research Letters*, 31, L09610,
777 doi:10.1029/2004GL019489.
- 778 Moore, D.E., and Lockner, D.A. (2011) Frictional strengths of talc-serpentine and
779 talc-quartz mixture. *Journal of Geophysical Research*, 116, B01403,
780 do:10.1029/2010JB007881.
- 781 Nakajima, J., Tsuji, Y., and Hasegawa, A. (2009) Seismic evidence for
782 thermally-controlled dehydration reaction in subduction oceanic crust. *Geophysical*
783 *Research Letters*, 36, L03303, doi:10.1029/2008GL036865.
- 784 Ohuchi, T., Lei, X.L., Ohfuji, H., Higo, Y., Tange, Y., Sakai, T., Fujino, K., and Irifune,
785 T. (2017) Intermediate-depth earthquakes linked to localized heating in dunite and
786 harzburgite. *Nature geoscience*, 10, 771-776.
- 787 Okazaki, K., and Hirth, G. (2016) Dehydration of lawsonite could directly trigger
788 earthquakes in subducting oceanic crust. *Nature*, 530, 81-84.
- 789 Okazaki, K., and Katayama, I. (2015) Slow stick slip of antigorite serpentinite under
790 hydrothermal conditions as a possible mechanism for slow earthquakes.
791 *Geophysical Research Letters*, 42, 1099-1104.
- 792 Omori, S., Komabayashi, T., and Maruyama, S. (2004) Dehydration and earthquakes in
793 the subducting slab: empirical link in intermediate and deep seismic zones. *Physics*
794 *of the Earth and Planetary Interiors*, 146(1), 297-311.
- 795 Padrón-Navarta, J.A., López Sánchez-Vizcaíno, V., Garrido, C.J., Gómez-Pugnaire, M.
796 T., Jabaloy, A., Capitani, G., and Mellini, M. (2008) Highly ordered antigorite from
797 Cerro del Almiraz HP-HT serpentinites, SE Spain. *Contributions to Mineralogy*

- 798 and Petrology, 156, 679-688.
- 799 Padrón-Navarta, J.A., López Sánchez-Vizcaíno, V., Hermann, J., Connolly, J.A.D.,
800 Garrido, C.J., Gómez-Pugnaire, M.T., and Marchesi, C. (2013) Tschermak's
801 substitution in antigorite and consequences for phase relations and water liberation
802 in high-grade serpentinites. *Lithos*, 178, 186-196.
- 803 Park, J.H., Yuan, Y., and Levin, V. (2004) Subduction zone anisotropy beneath
804 Corvallis, Oregon: A serpentinite skid mark of trench-parallel terrane migration?
805 *Journal of Geophysical Research*, 109, B10306, doi:10.1029/2003JB002718.
- 806 Peacock, S.M. (2001) Are the lower planes of double seismic zones caused by
807 serpentine dehydration in abducting oceanic mantle? *Geology*, 29(4), 299-302.
- 808 Peacock, S.M., and Wang, K. (1999) Seismic consequences of warm versus cool
809 subduction metamorphism: Examples from Southwest and Northeast Japan.
810 *Science*, 286, 937-939.
- 811 Perrillat, J.-P., Daniel, I., Koga, K.T., Reynard, B., Cardon, H., and Crichton, W.A.
812 (2005) Kinetics of antigorite dehydration: A real-time X-ray diffraction study. *Earth
813 and Planetary Science Letters*, 236, 899-913.
- 814 Proctor, B., and Hirth, G. (2015) Role of pore fluid pressure on transient strength
815 changes and fabric development during serpentine dehydration at mantle
816 conditions: Implications for subduction-zone seismicity. *Earth and Planetary
817 Science Letters*, 421, 1-12.
- 818 Raleigh, C.B., and Paterson, M.S. (1965) Experimental deformation of serpentinite and
819 its tectonic implications. *Journal of Geophysical Research*, 70, 3965-3985.

- 820 Rayner, J.H., and Brown, G. (1973) The crystal structure of talc. *Clays Clay Miner.*, 21,
821 103-114.
- 822 Reynard, B. (2013) Serpentine in active subduction zones. *Lithos*, 178, 171-185.
- 823 Reynard, B., Hilairet, N., Balan, E., and Lazzeri, M. (2007) Elasticity of serpentines
824 and extensive serpentinization in subduction zones. *Geophysical Research Letters*,
825 34(13), L13307, doi:10.1029/2007GL030176.
- 826 Reynard, B., Nakajima, J., and Kawakatsu, H. (2010) Earthquakes and plastic
827 deformation of anhydrous slab mantle in double Wadati-Benioff zones.
828 *Geophysical Research Letters*, 37, L24309, doi:10.1029/2010GL045494.
- 829 Rinaudo, C., and Gastaldi, D. (2003) Characterization of chrysotile, antigorite and
830 lizardite by FT-RAMAN spectroscopy. *The Canadian Mineralogist*, 41, 883-890.
- 831 Rubie, D.C., and Thompson, A.B. (1985) Kinetics of metamorphic reactions at
832 elevated temperatures and pressures: An appraisal of available experimental data.
833 In Thompson, A.B., and Rubie, D.C. (Eds.) *Metamorphic Reactions: Kinetics,*
834 *Textures, and Deformation*, p. 27-29. Springer.
- 835 Rutter, E.H., and Brodie, K.H. (1988) Experimental “syntectonic” dehydration of
836 serpentinite under conditions of controlled pore water pressure. *Journal of*
837 *Geophysical Research*, 93(B5), 4907-4932.
- 838 Sawai, M., Katayama, I., Hamada, A., Maeda, M., and Nakashima, S. (2013)
839 Dehydration kinetics of antigorite using in situ high-temperature infrared
840 microspectroscopy. *Physics and Chemistry of Minerals*, 40, 319-330.
- 841 Scambelluri, M., Muentener, O., Hermann, J., Piccardo, G.B., and Trommsdorff, V.

- 842 (1995) Subduction of water into the mantle: History of an Alpine peridotite.
843 *Geology*, 23, 459-462.
- 844 Schmidt, M.W., and Poli, S. (1998) Experimentally based water budgets for
845 dehydrating slabs and consequences for arc magma generation. *Earth and Planetary*
846 *Science Letters*, 163(1), 361-379.
- 847 Schubnel, A., Brunet, F., Hilairet, N., Gasc, J., Wang, Y., and Green, H.W. (2013)
848 Deep-focus earthquake analogs recorded at high pressure and temperature in the
849 laboratory. *Science*, 341(6152), 1377-1380.
- 850 Shao, T., Ji, S., Kondo, Y., Michibayashi, K., Wang, Q., Xu, Z., Sun, S., Marcotte, D.,
851 and Salisbury, M.H. (2014) Antigorite-induced seismic anisotropy and implications
852 for deformation in subduction zones and the Tibetan Plateau. *Journal of*
853 *Geophysical Research*, 119(3), 2068-2099.
- 854 Shao, T., Zhou, Y., Song, M., Ma, X., Zhang, L., Yao, W., Dang, J., and Li, J.F. (2021)
855 Deformation of antigorite and its geological implications. *Journal of Geophysical*
856 *Research*, 126, <https://doi.org/10.1029/2021JB021650>.
- 857 Shen, T.T., Zhang, C., Chen, J., Hermann, J., Zhang, L.F., Pardron-Navarta, J.A., Chen,
858 L., Xu, J., and Yang, J.S. (2020) Changes in the cell parameters of antigorite close
859 to its dehydration reaction at subduction zone conditions. *American Mineralogist*,
860 105, 569-582.
- 861 Song, T.R.A., Helmberger, D.V., Brudzinski, M.R., Clayton, R.W., Davis, P.,
862 Perez-Campos, X., and Singh, S.K. (2009) Subducting slab ultra-slow velocity
863 layer coincident with silent earthquakes in Southern Mexico. *Science*, 324,

- 864 502-506.
- 865 Soyer, W., and Unsworth, M. (2006) Deep electrical structure of the northern Cascadia
866 (British Columbia, Canada) subduction zone: Implications for the distribution of
867 fluids. *Geology*, 34(1), 53-56.
- 868 Syracuse, E.M., van Keken, P.E., and Abers, G.A. (2010) The global range of
869 subduction zone thermal models. *Physics of the Earth and Planetary Interiors*, 183,
870 73-90.
- 871 Takahashi, M., Uehara, S.-I., Mizoguchi, K., Shimizu, I., Okazaki, K., and Masuda, K.
872 (2011) On the transient response of serpentine (antigorite) gouge to stepwise
873 changes in slip velocity under high-temperature conditions. *Journal of Geophysical*
874 *Research*, 116, B10405, doi:10.1029/2010JB008062.
- 875 Taylor, L.S., and York, P. (1998) Effect of particle size and temperature on the
876 dehydration kinetics of trehalose dehydrate. *International Journal of Pharmaceutics*,
877 167, 215-221.
- 878 Trittschack, R., and Grobéty, B. (2012) Dehydroxylation kinetics of lizardite. *European*
879 *Journal of Mineralogy*, 24(1), 47-57.
- 880 Trittschack, R., Grobéty, B., and Brodard, P. (2014). Kinetics of the chrysotile and
881 brucite dihydroxylation reaction: a combined non-isothermal/isothermal
882 thermogravimetric analysis and high-temperature X-ray powder diffraction study.
883 *Physics and Chemistry of Minerals*, 41(3), 197-214.
- 884 Ulmer, P., and Trommsdorff, V. (1995) Serpentine stability to mantle depths and
885 subduction-related magmatism. *Science*, 268, 858-860.

- 886 Ulmer, P., and Trommsdorff, V. (1999) Phase relations of hydrous mantle subducting to
887 300 km. Conference Paper, Geochemical Society, Houston, pp. 259-282.
- 888 Wang, D., Liu, X., Liu, T., Shen, K., Welch, D.O., and Li, B. (2017) Constraints from
889 the dehydration of antigorite on high-conductivity anomalies in subduction zones.
890 Scientific Reports, 7(1), 16893, doi:10.1038/s41598-017-16883-4.
- 891 Wang, D., Wang, Y., Yi, L., and Huang, B. (2015). Dehydration kinetics of natural talc.
892 Canadian Mineralogist, 53(4), 643-651.
- 893 Weber, J.N., and Greer, R.T. (1965) Dehydration of serpentine: Heat of reaction and
894 reaction kinetics at $P_{\text{H}_2\text{O}} = 1$ atm. American Mineralogist, 50, 450-464.
- 895 Wunder, B., Baronnet, A., and Schreyer, W. (1997) Ab-initio synthesis and TEM
896 confirmation of antigorite in the system MgO-SiO₂-H₂O. American Mineralogist,
897 82, 760-764.
- 898 Wunder, B., and Schreyer, W. (1997) Antigorite: high-pressure stability in the system
899 MgO-SiO₂-H₂O (MSH). Lithos, 41, 213-227.
- 900 Wunder, B., Wirth, R., and Gottschalk, M. (2001) Antigorite: Pressure and temperature
901 dependence of polysomatism and water content. European Journal of Mineralogy,
902 13, 485-495.
- 903 Xia, G. (2013) Experimental studies on dehydration embrittlement of serpentinized
904 peridotite and effect of pressure on creep of olivine. Ph.D. Dissertation, *Riverside:*
905 *University of California.*
- 906 Yamaguchi, S., Uyeshima, M., Murakami, H., Sutoh, S., Tanigawa, D., Ogawa, T.,
907 Oshiman, N., Yoshimura, R., Aizawa, K., Shiozaki, I., and Kasaya, T. (2009)

- 908 Modification of the Network-MT method and its first application in imaging the
909 deep conductivity structure beneath the Kii Peninsula, southwestern Japan. *Earth,*
910 *Planets and Space*, 61, 957-971.
- 911 Yamasaki, T., and Seno, T. (2003) Double seismic zone and dehydration embrittlement
912 of the subducting slab. *Journal of Geophysical Research*, 108(B4),
913 doi:10.1029/2002JB001918.
- 914 Zhang, Z., and Duan, Z. (2005) Prediction of the PVT properties of water over wide
915 range of temperatures and pressures from molecular dynamics simulation. *Physics*
916 *of the Earth and Planetary Interior*, 149, 335-354.
- 917 Zhou, S., Wei, Y., Li, B., Ma, B., Wang, C., and Wang, H. (2017) Kinetics study on the
918 dihydroxylation and phase transformation of $Mg_3Si_2O_5(OH)_4$. *Journal of Alloys*
919 *and Compounds*, 713, 180-186.

920

Figure and table captions

921

922 **Figure 1.** High-resolution TEM image of the starting material (a) and histogram of m
923 values showing the distribution of periodicities (b)

924

925 **Figure 2.** Schematics of a Tuttle-type autoclave (cold-seal hydrothermal vessel)
926 employed for the high- PT experiments in this study

927

928 **Figure 3.** Comparison of XRD patterns of experimental products over time for
929 representative samples under the initially water-unsaturated conditions of 200 MPa
930 confining pressure and 600 °C temperature. Below the graph are the PDF cards of talc
931 (Rayner and Brown, 1973), forsterite (Hushur et al., 2009) and antigorite (Hess et al.,
932 1952). Atg = antigorite, Fo = forsterite, and Tlc = talc.

933

934 **Figure 4.** Variations in decomposition of antigorite and crystallization of forsterite and
935 talc (wt.%) with time (min) for the dehydration reaction of antigorite to forsterite + talc
936 at 600 (a), 625 (b), and 650 °C (c and d). Panels a-c display data under initially
937 water-unsaturated conditions, while panel d shows data under water-saturated
938 conditions. Vertical line represents error.

939

940 **Figure 5.** Plots of $\ln[-\ln(1-\alpha)]$ versus $\ln(t)$ for each solid phase involved in reaction (1)
941 at 600, 625, and 650 °C. Decomposition of antigorite (a, d) and crystallization of

942 forsterite (b) and talc (c) occur in reaction (1). Reactions shown in panels a-c are under
943 initially water-unsaturated conditions, while those shown in panel d are under
944 water-saturated conditions. The slopes of the lines fit to the data points marked by
945 hollow circles represent the n values that best describe the reaction mechanisms. Data
946 points marked by solid circles have not been included for the fitting due to large errors.

947

948 **Figure 6.** Arrhenius diagram of the dehydration of antigorite. As shown in this figure,
949 the activation energy, E , can be calculated from the slope of the solid line.

950

951 **Figure 7.** PT conditions of the present experiments (red stars) and a MgO-SiO₂-H₂O
952 (MSH) phase diagram constructed with a blue line, black line, pink line and red dashed
953 line representing the phase boundaries defined by the data of Evans et al. (1976),
954 Ulmer and Trommsdorff (1995), Wunder and Schreyer (1997) and Perrillat et al.
955 (2005), respectively. The phase boundary represented by the red dashed line
956 corresponds to low water activity. Magenta dotted lines delimit PT ranges for different
957 m -isolines of synthetic antigorite, which are labeled by magenta italic numbers, in the
958 MSH system determined by Wunder et al. (2001). The yellow vertical bar with
959 $m=14-15$ represents natural antigorite from Cerro del Almirez, Spain (Padrón-Navarta
960 et al., 2008). The blue horizontal bar with $m=15-16$ is shown for natural antigorite
961 from central Cuba (Auzende et al., 2002). Circles show the PT conditions at
962 hypocenters calculated by Abers et al. (2013) for seismicity in the subducting mantle

963 beneath southwestern Japan [Kii (pink circle), Tokai (green circle)] and Cascadia (blue
964 circle). Hollow stars indicate the starting material (i.e., antigorite) with the most
965 frequently observed $m=15$ (Figure 1), which is stable and undecomposed under the
966 corresponding PT conditions, and solid stars indicate the occurrence of dehydration of
967 the starting material to produce forsterite + talc under the corresponding PT conditions.
968 Atg = antigorite, Fo = forsterite, Tlc = talc, and En = enstatite.

969

970 **Figure 8.** BSE images of recovered run products. (a) Atg103 under 600 °C and initially
971 water-unsaturated conditions for 48 h. (b) Atg112 under 650 °C and water-saturated
972 conditions for 3 h.

973

974 **Figure 9.** Dehydration kinetic models for antigorite at 600 and 650 °C, corresponding
975 to the endmember isotherms bounding the hypocenters of the lower-plane seismicity of
976 a DSZ, derived from the parameters of isothermal experiments. Models for antigorite
977 dehydration kinetics at 625 °C and initially water-unsaturated conditions and at 650 °C
978 and water-saturated conditions are also included for comparisons. A solid line
979 represents an initially water-unsaturated model, while a dashed line shows a
980 water-saturated model. The hollow circles represent the experimental data used for
981 fitting n and k that are used to stimulate the kinetic curves, while the data marked by
982 solid circles are not included for fitting. Vertical line represents the degree of deviation
983 of data from the curve, which can be used to constrain the error of the data.

Table 1. Experimental conditions and results for dehydration kinetics of antigorite at a constant pressure of 20 type autoclave

Sample #	Temperature (°C)	Duration (h)	Dehydration	Recovered products (wt.%)*			
				Antigorite	Error ^{&}	Forsterite	Error
Atg3	650	18	Yes	0.00	0.00	50.30	(31.10)
Atg4	650	3	Yes	41.40	(19.76)	7.60	3.75
Atg5	650	1	Yes	94.20	(19.78)	1.70	(0.58)
Atg7	550	6	No	100.00	0.00	0.00	0.00
Atg8	500	240	No	100.00	0.00	0.00	0.00
Atg10	650	15	Yes	0.00	0.00	14.20	(5.02)
Atg11	500	745.5	No	100.00	0.00	0.00	0.00
Atg12	650	9	Yes	2.00	(1.96)	18.20	0.78
Atg21	650	4.5	Yes	4.10	1.93	19.20	(0.62)
Atg22	650	6	Yes	3.00	(1.67)	21.20	(2.41)
Atg23	650	12	Yes	0.10	(0.10)	55.60	(36.40)
Atg26	600	9	Yes	91.00	(2.71)	7.00	(2.86)
Atg27	600	15	Yes	81.00	(2.81)	11.00	0.03
Atg28	600	36	Yes	39.00	6.41	29.00	4.37
Atg29	600	48	Yes	54.90	(23.49)	15.60	23.56
Atg31	600	6	No	100.00	(7.00)	0.00	0.00
Atg32	600	24	Yes	79.92	(16.79)	6.70	11.76
Atg33	600	60	Yes	21.00	0.04	49.00	(7.50)
Atg35	600	84	Yes	17.00	(8.29)	54.00	(11.26)
Atg36	650	10.5	Yes	0.00	0.00	46.09	(26.90)
Atg41	600	72	Yes	25.00	(11.30)	45.00	(2.81)
Atg50	600	120	Yes	26.00	(24.03)	38.00	5.29
Atg52	650	20	Yes	0.00	0.00	51.49	(32.30)
Atg54	580	360	Yes	67.06	4.20	14.91	0.22
Atg55	565	360	No	100.00	0.00	0.00	0.00
^s Atg57	650	3	Yes	94.70	(2.77)	5.30	(2.10)
^s Atg58	650	6	Yes	86.70	(3.88)	6.30	1.73
^s Atg59	650	9	Yes	81.10	(7.18)	8.60	2.82
^s Atg60	650	15	Yes	69.70	(11.87)	15.30	3.00
^s Atg61	650	48	Yes	14.80	(2.80)	53.30	(1.83)
Atg88	625	36	Yes	0.00	0.53	55.10	2.31
Atg89	625	24	Yes	9.90	(4.76)	51.70	0.03
Atg90	625	15	Yes	16.40	5.09	50.10	(2.11)
Atg91	625	6	Yes	71.10	(5.84)	16.90	(0.31)
Atg92	625	3	Yes	82.60	2.45	12.40	(2.41)
Atg93	625	1	Yes	95.50	1.08	4.00	(1.42)

*Uncertainties in quantitative phase analysis may mainly result from the preferred orientation of both antigorite grain morphology and size of three phases in the run products.

[&]Error is constrained by the degree of deviation of decomposed antigorite data from the isothermal kinetic curve.
^sWater-saturated conditions.

0 MPa using a Tuttle-

Talc	Error
49.70	31.08
51.00	(3.75)
4.10	0.58
0.00	0.00
0.00	0.00
85.80	(5.02)
0.00	0.00
79.80	(0.79)
76.70	0.62
75.80	2.41
44.30	36.38
3.00	0.00
8.00	0.00
32.00	(7.80)
29.40	(1.00)
0.00	0.00
13.39	0.00
30.00	0.10
29.00	2.00
53.91	26.87
30.00	0.60
37.00	(5.60)
48.51	32.28
18.00	(4.42)
0.00	0.00
0.00	2.10
7.00	(1.73)
10.30	(2.82)
15.00	(3.00)
31.90	1.83
44.90	(2.38)
38.40	(0.09)
33.50	2.05
11.40	0.89
5.00	2.40
0.50	1.41

e and talc and the

ve.

Table 2. Information on kinetic mechanism parameters for dehydration of antigorite and crystallization

Phase	T (°C)	n	$\ln k$	R^2
Antigorite	600	1.33 ± 0.13	-15.92 ± 1.49	0.97
	625	1.40 ± 0.02	-14.83 ± 0.38	0.93
	650	1.50 ± 0.02	-13.50 ± 0.38	0.79
	650*	1.16 ± 0.08	-13.29 ± 0.92	0.98
Forsterite	600	1.37 ± 0.08	-15.84 ± 0.90	0.99
	625	1.24 ± 0.01	-13.21 ± 0.19	0.97
	650	1.15 ± 0.18	-11.19 ± 1.67	0.95
Talc	600	2.68 ± 0.20	-30.43 ± 2.18	0.99
	625	2.71 ± 0.05	-26.88 ± 0.89	0.81
	650	2.67 ± 0.00	-24.58 ± 0.03	1.00

*Water-saturated conditions

of forsterite and talc

Table 3. Activation energies of the dehydration of antigorite from the literature

Activation energy (kJ/mol)	Comment	Methods
268.1	slow dehydration	thermogravimetric analysis and 2-DAEM
299.2	fast dehydration	
400		thermogravimetric analysis and Flynn-Wall-Oza
219	water band 1	in situ high-temperature infrared spectroscopy
243	water band 2	
256	water band 3	
255	612-708 °C	in situ powder XRD and TEM
444-728	689-766 °C	thermogravimetric analysis and XRD

References

Liu et al. (2019)

Sawai et al. (2013)

Gualtier et al. (2012)

Weber and Greer (1965)

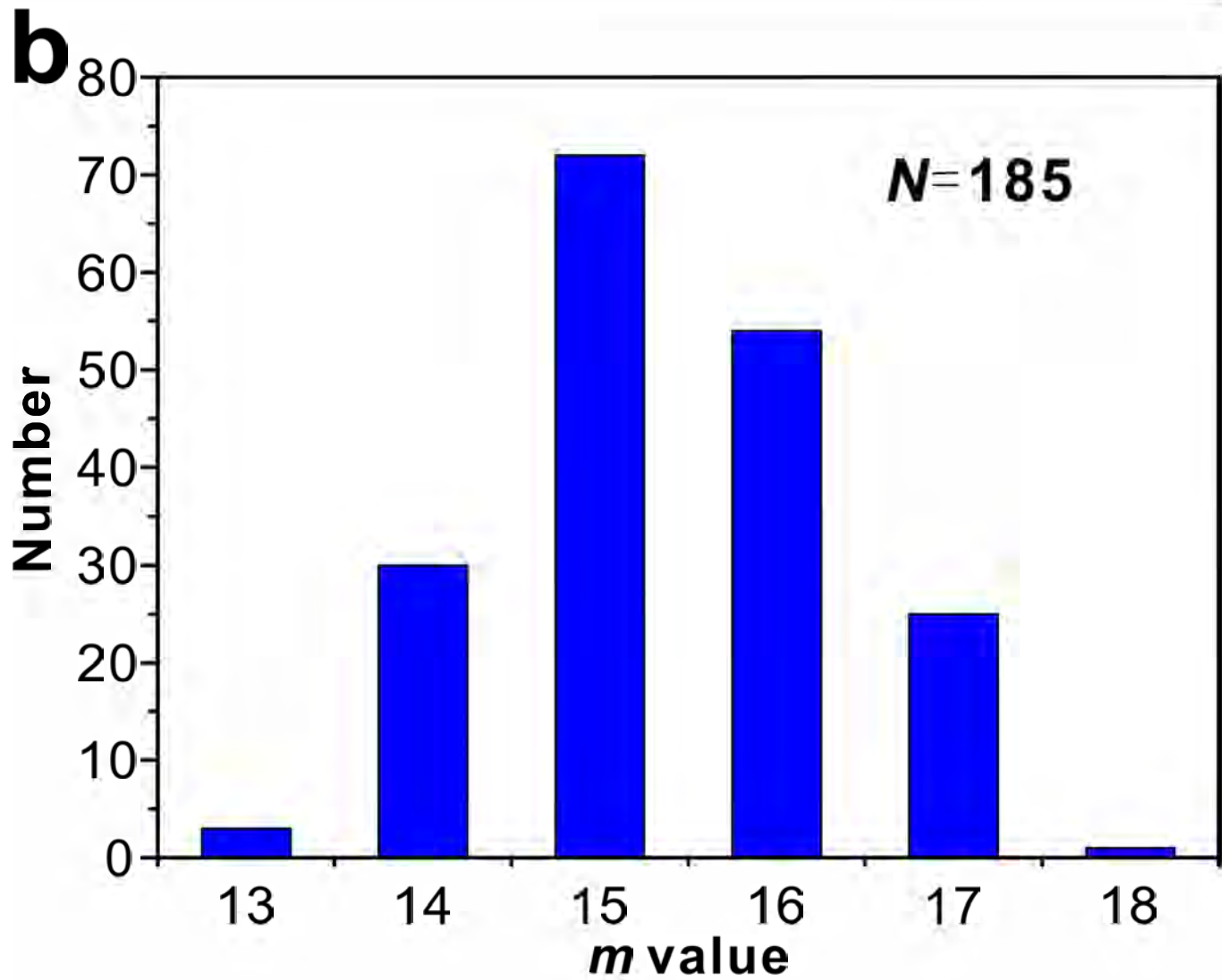
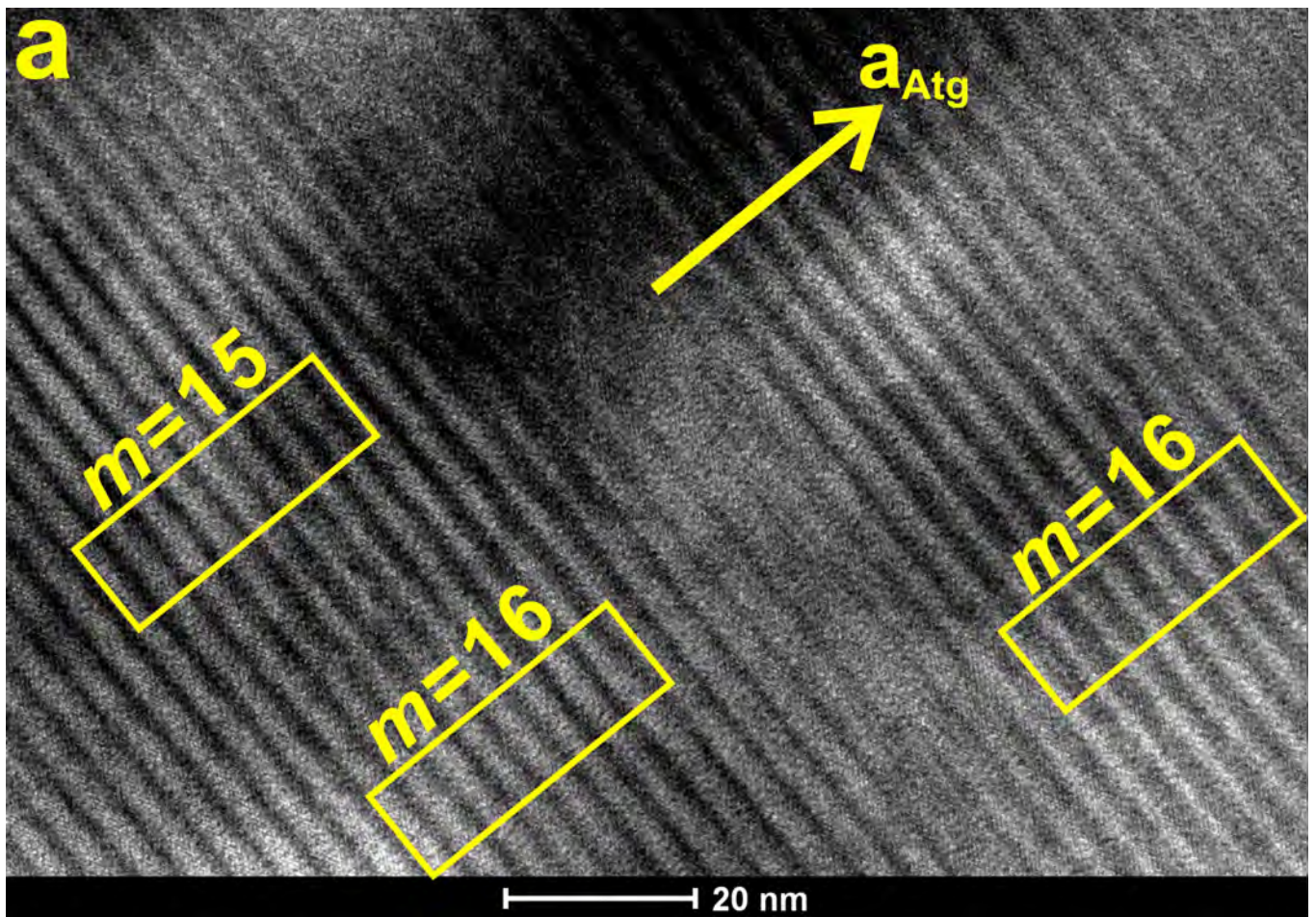


Figure 1

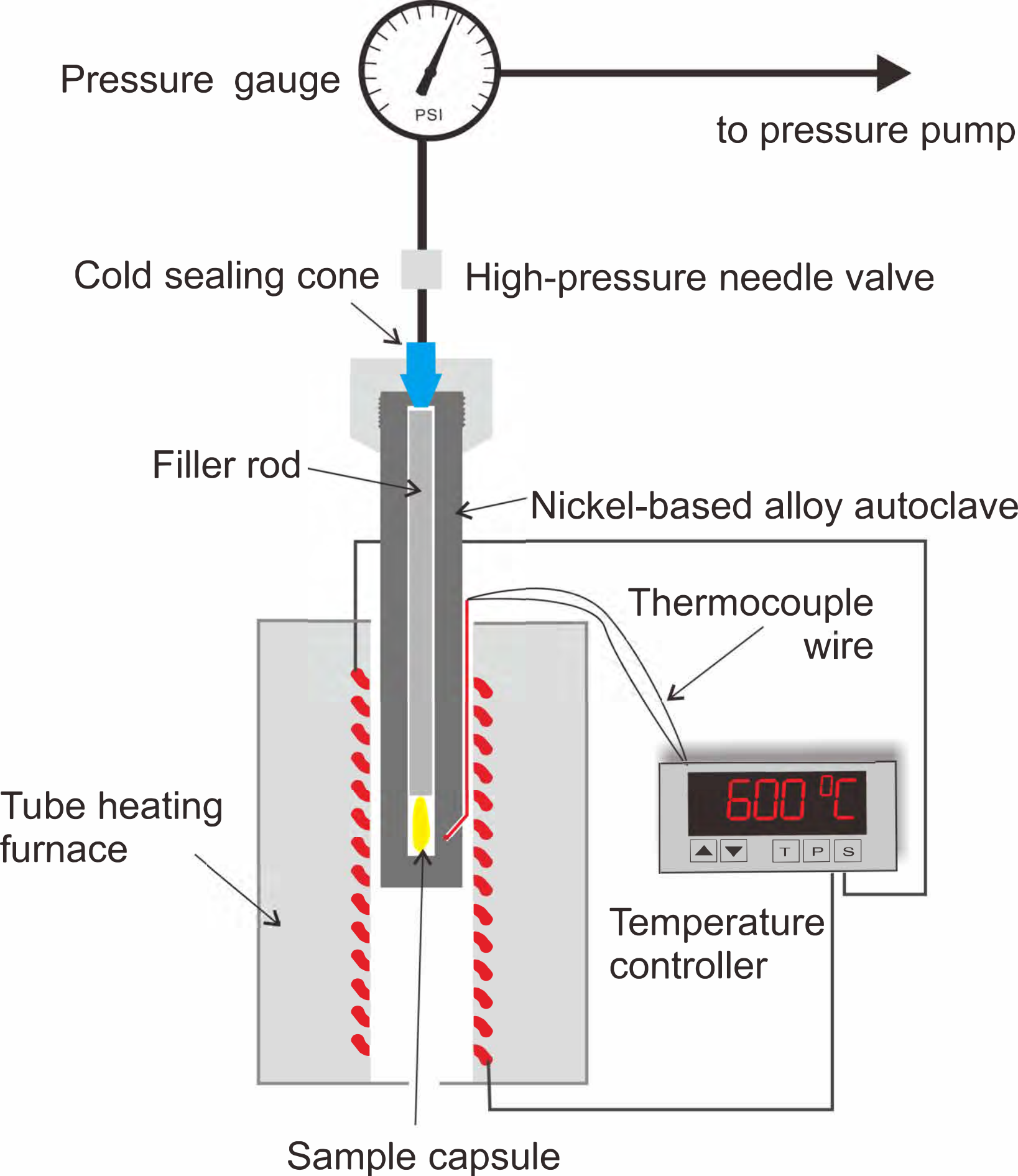


Figure 2

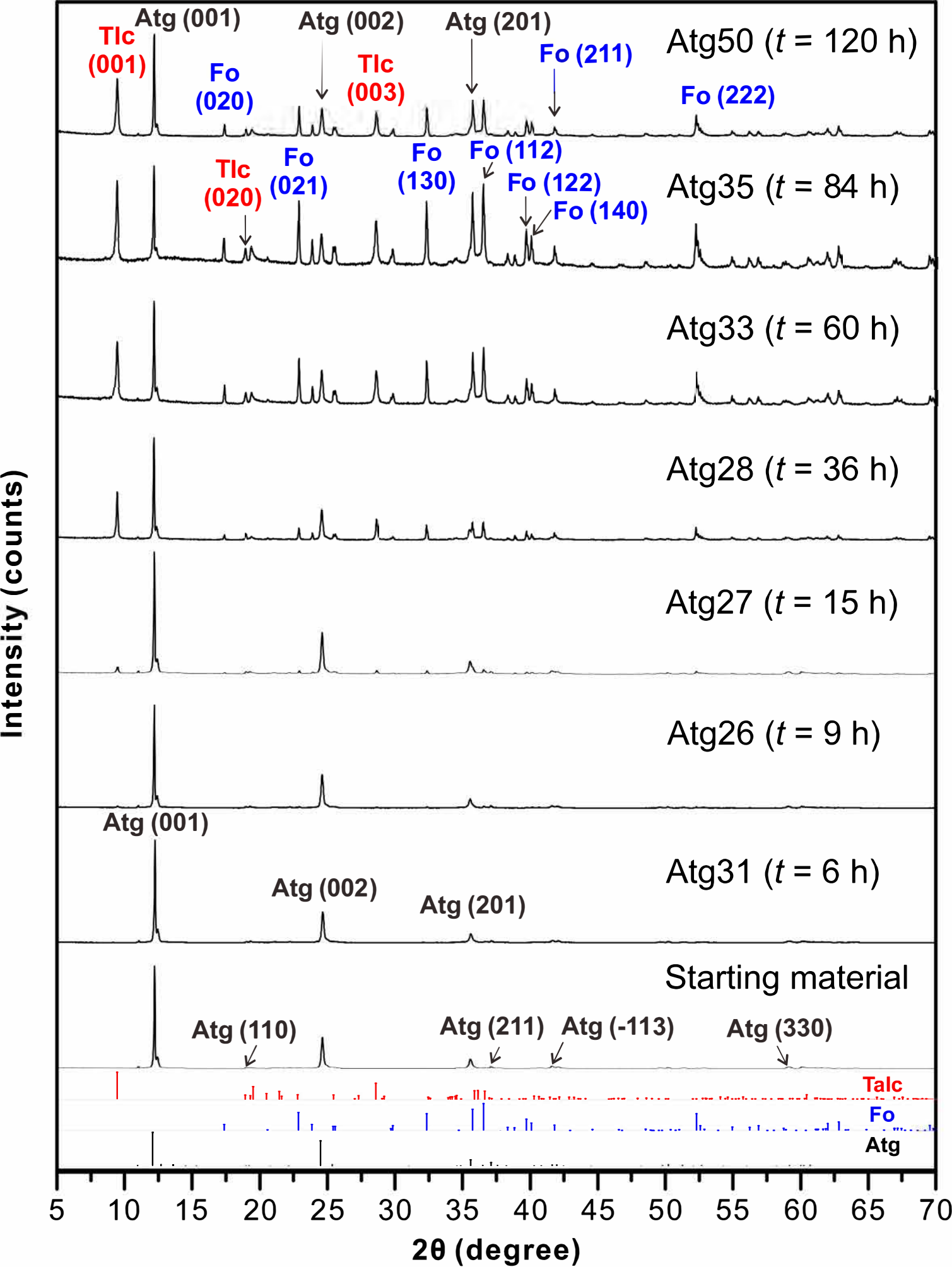


Figure 3

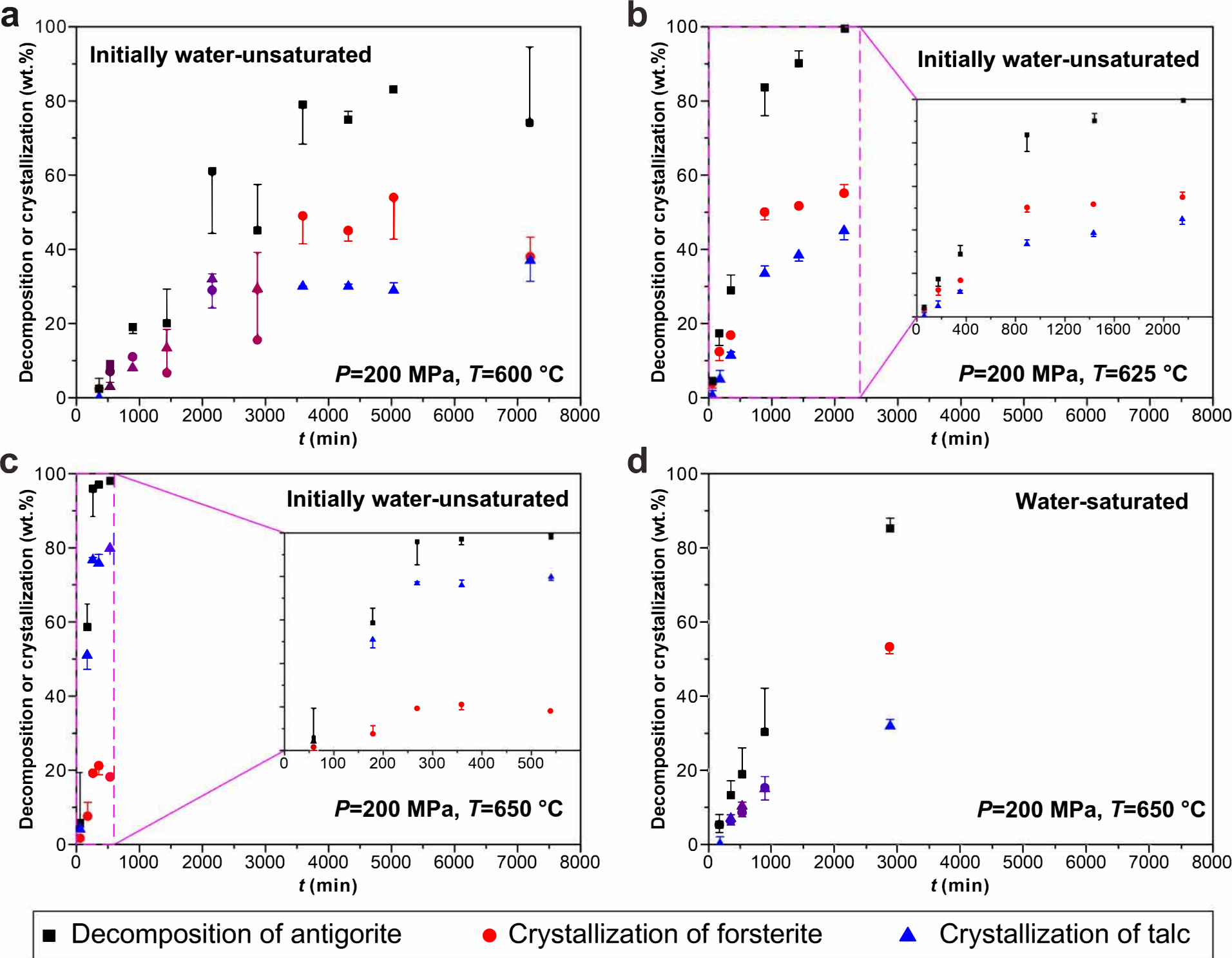


Figure 4

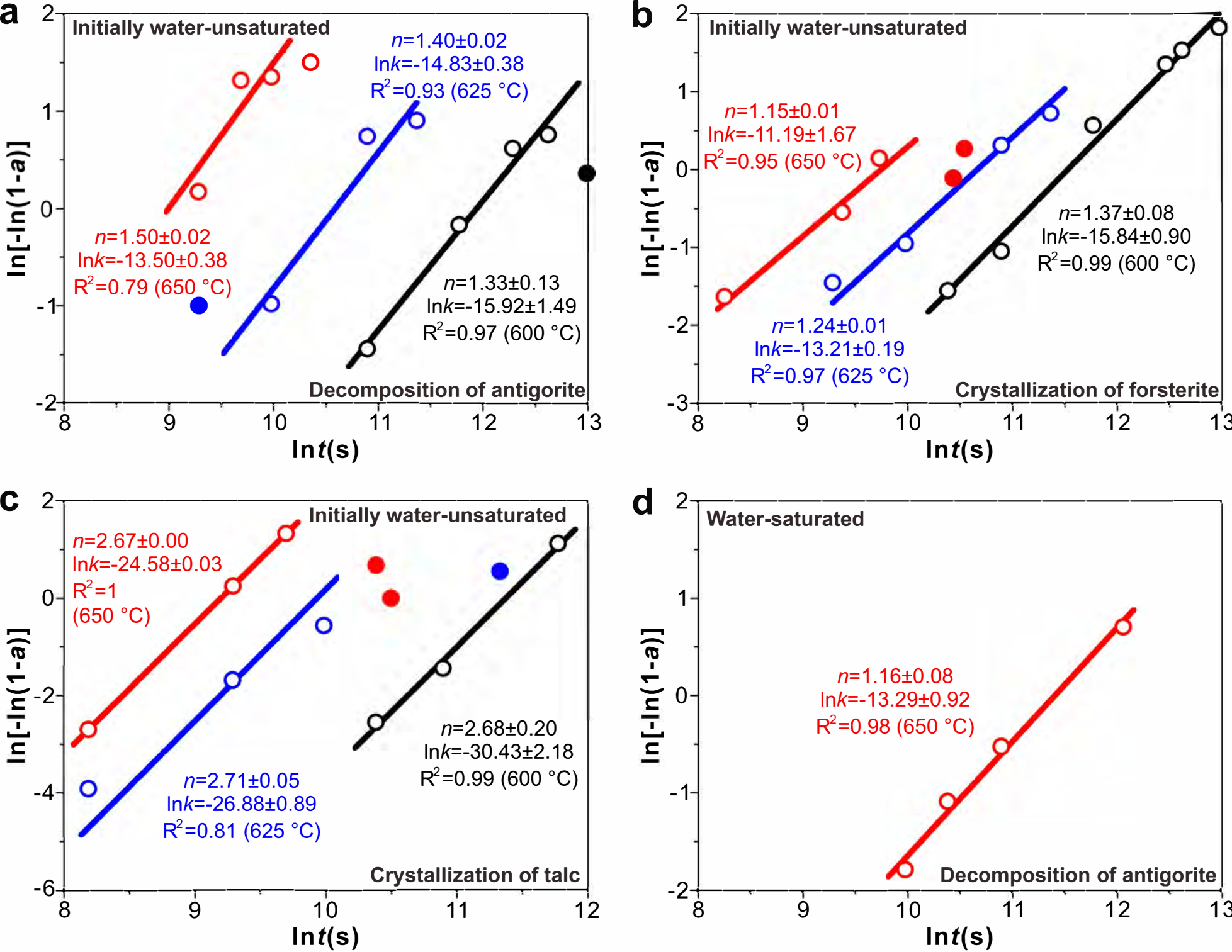


Figure 5

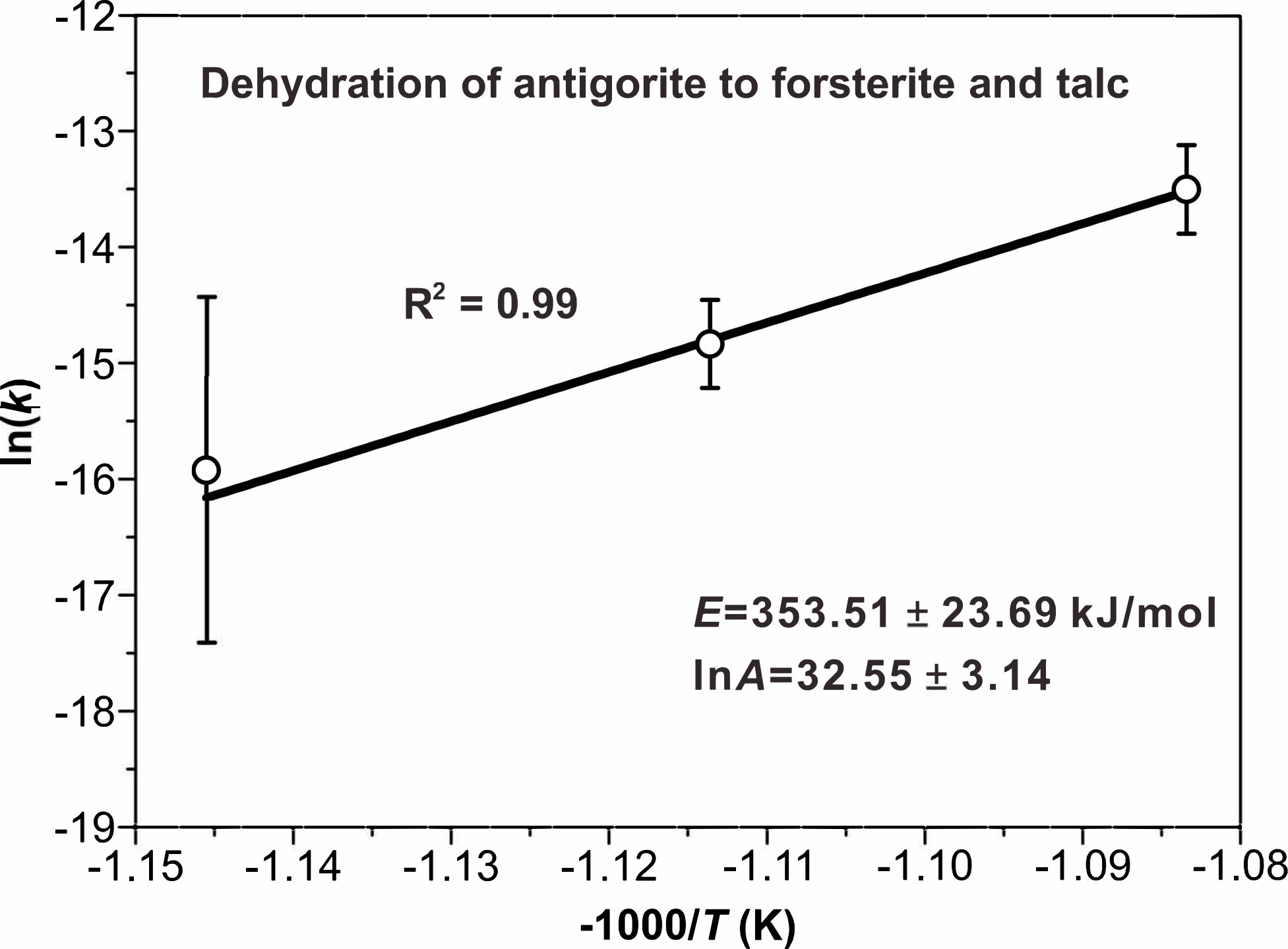


Figure 6

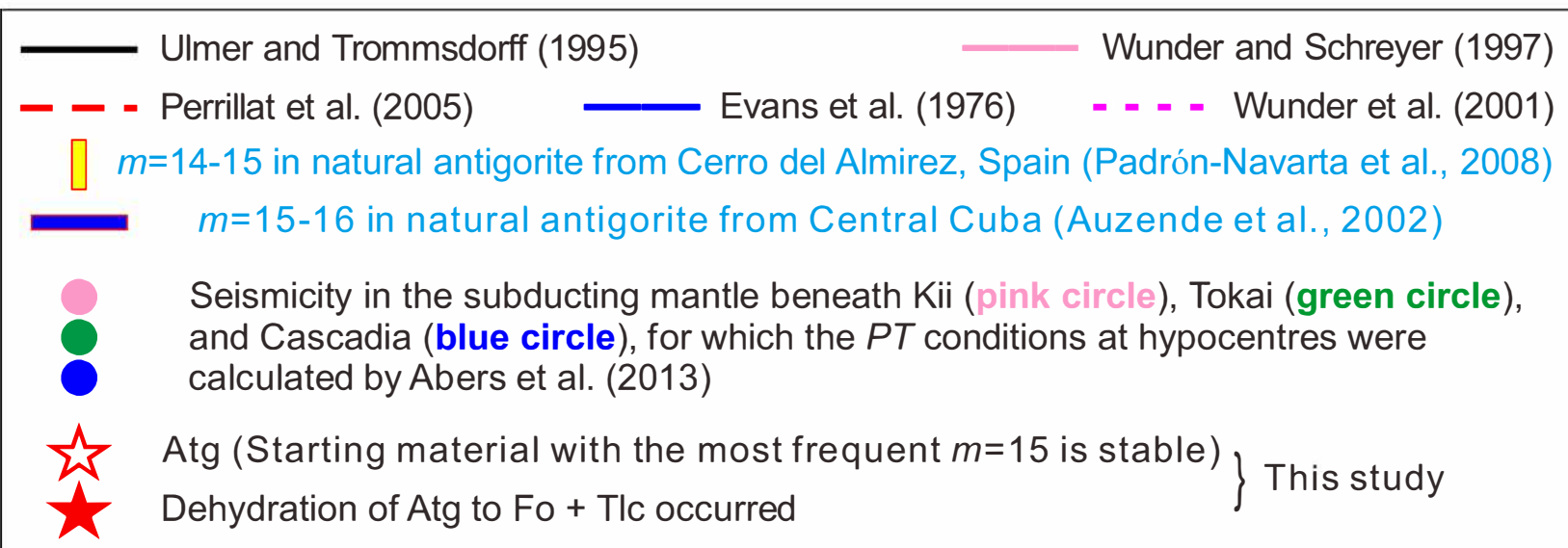
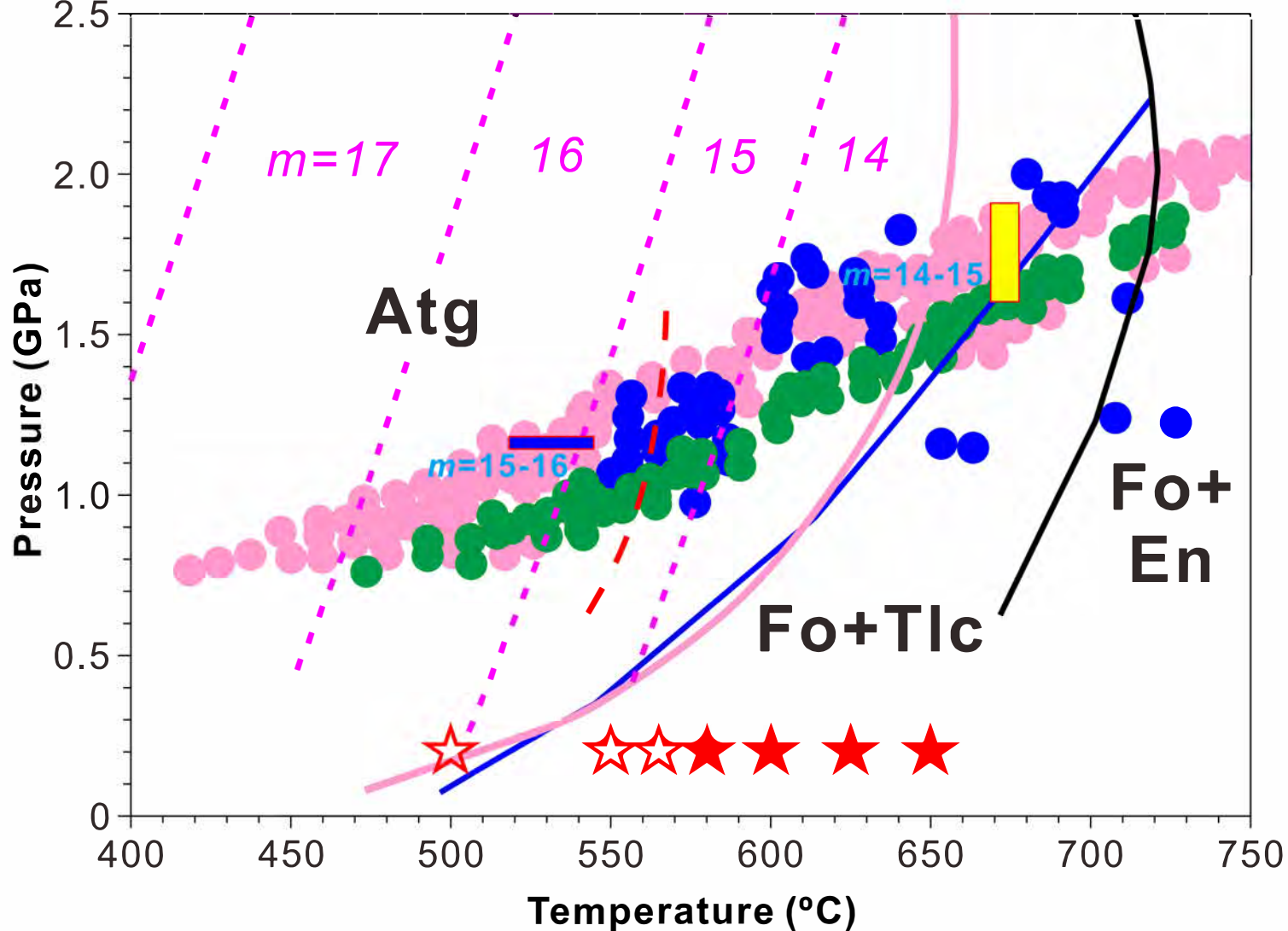


Figure 7

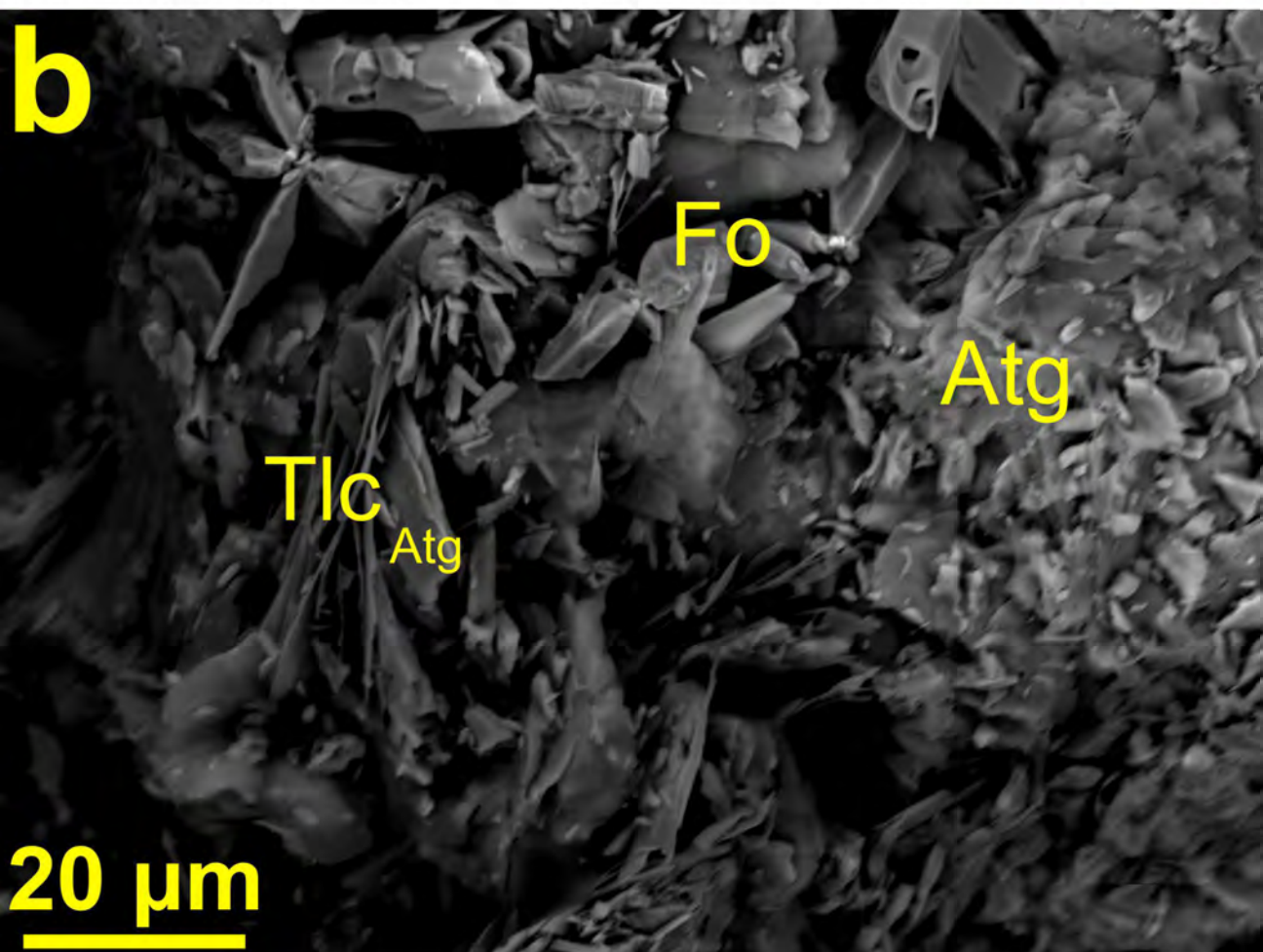
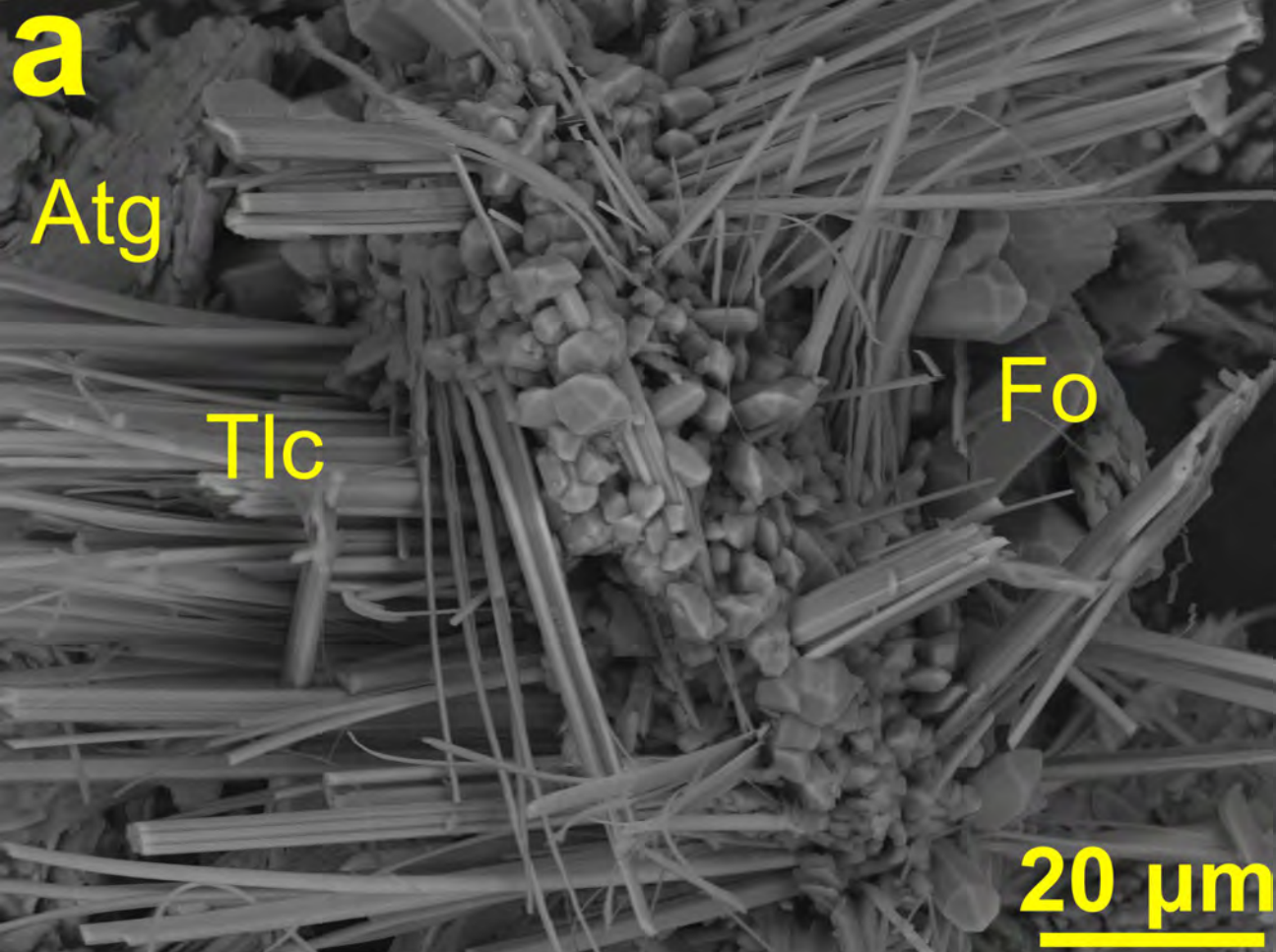


Figure 8

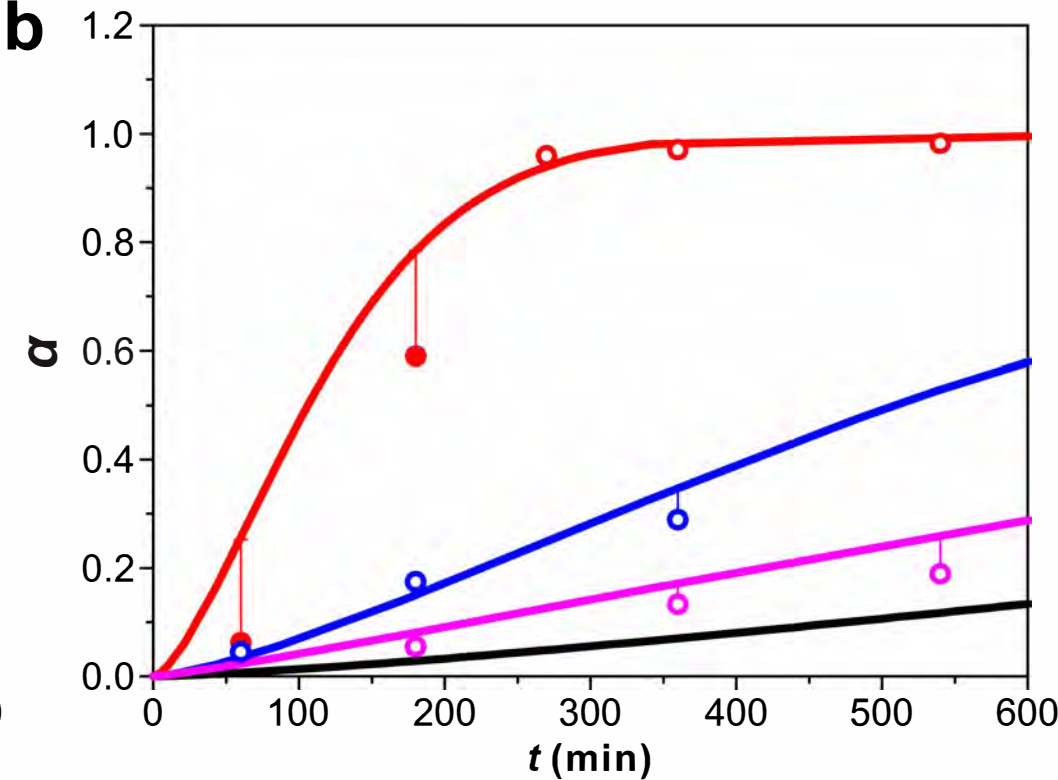
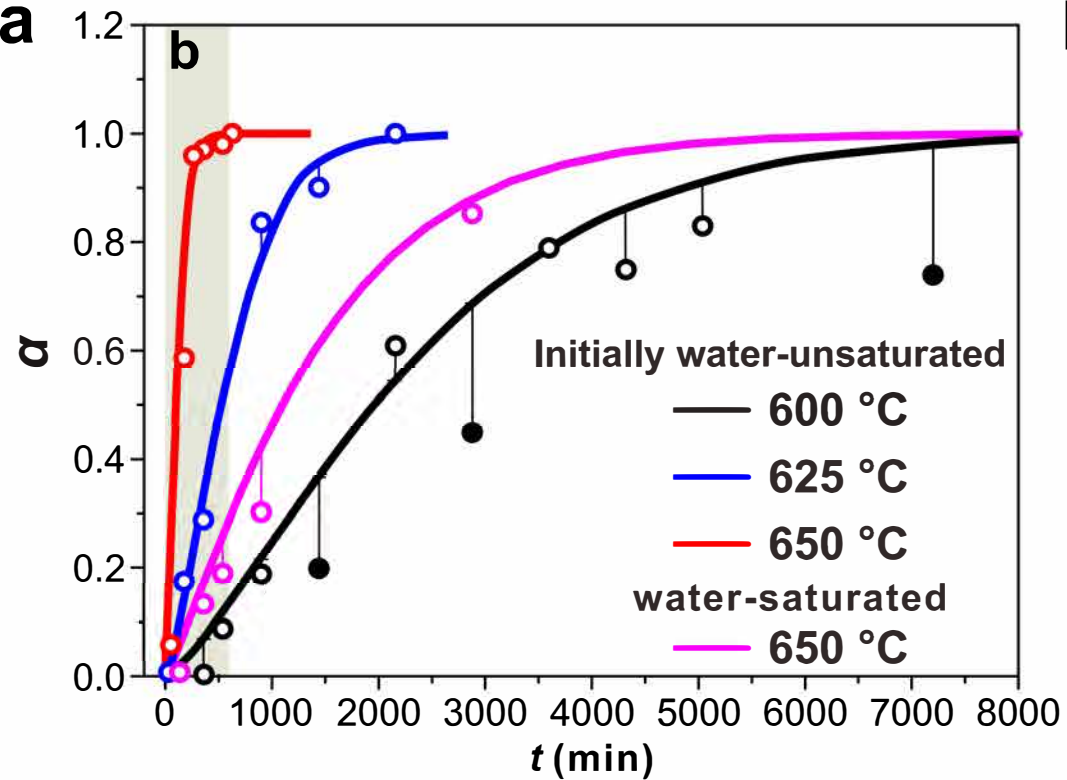


Figure 9